Filament Path Optimization of Fused Filament Fabricated Parts Incorporating the Effect of Pre-Fusion Densities

Varun Murugan[a,b,*], Gianluca Alaimo[a], Stefania Marconi[a], Peter Z. Berke[b], Thierry J. Massart[b], Ferdinando Auricchio[a]

[a]*Department of Civil Engineering and Architecture, University of Pavia, via Ferrata 3, 27100 Pavia, Italy*
[b]*Building Architecture and Town Planning Department, Université Libre de Bruxelles (ULB), avenue F.D. Roosevelt 50, 1050 Brussels, Belgium*

Abstract

Fused Filament Fabricated parts exhibit mechanical anisotropy induced by the filament extrusion pattern and possibly due to the intrinsic nature of feedstock material. Consequently, an optimized filament deposition strategy is desirable for improving the part's functionality. The present work optimizes the in-plane filament paths of Fused Filament Fabricated parts to strengthen component load-bearing capacity, with a particular focus on obtaining production-ready design solutions through a direct imposition of the manufacturing constraints. To perform an effective in-plane filament path optimization, the present contribution also addresses, among several other aspects, the following: (i) the development and implementation of a new material model that incorporates the transverse stiffness loss before inter-filament fusion, and (ii) a comparative study between a two-step gradient-

---

[*]Corresponding author
Email address: `varunmurugan93@gmail.com` (Varun Murugan)

based minimization and a global metaheuristic minimization. The results indicate that the new material model yields more realistic filament patterns compared to the assumption of neglecting the transverse stiffness loss at low filament densities. Further, the comparison of optimization approaches suggests the preference for the two-step gradient-based approach due to its better efficiency, flexibility, and compatibility with the proposed material model.

Keywords: Additive Manufacturing, Fused Filament Fabrication, filament path optimization, anisotropic material model, curvilinear filaments

1. Introduction

3D-Printing, formally known as Additive Manufacturing (AM), is a generic term for fabrication techniques that produce complex three-dimensional objects by adding material in a layer-wise manner. Among the various AM technologies (Vyavahare et al. (2020)), Fused Filament Fabrication (FFF) can rapidly produce a physical replica of a digital model by extruding layers of molten thermoplastic filaments along predetermined paths (Monaldo and Marfia (2021)). Reduced lead times, no tooling requirements, ease of use, and economic accessibility are some of the characteristics of FFF (Cuan-Urquizo et al. (2019)) that make such technology suitable for prototyping purposes. Nevertheless, recent trends focus on extending FFF from prototyping to more valuable industrial applications through effective design tools that exploit the FFF features (Hoglund and Smith (2016); Tam and Mueller (2017); Khan et al. (2018)).

The mechanical response of FFF parts displays strong dependence on the direction of the deposited filaments i.e., the filament deposition process induces anisotropic behaviour, with increased stiffness and strength along the filament directions (Rodríguez et al. (2001); Ahn et al. (2002); Li et al. (2002); Durgun and Ertan (2014); Alaimo et al. (2017)). On top of that, anisotropy may also be caused by the intrinsic nature of the feedstock material, for instance, when reinforced polymer matrix composites are used (Tekinalp et al. (2014); Blok et al. (2018); Brenken et al. (2018)). Therefore, regardless of the source of anisotropy, it is beneficial to avoid the arbitrary filament deposition strategy as generally adopted by standard slicing software (Hodgson et al. (2011)), and instead optimize the filament deposition paths to reach superior

3

structural performance (like stiffness and strength, among others).

The present work aims at contributing to the filament path optimization of load-bearing FFF structures for maximizing their stiffness. A number of studies in the literature successfully employed optimization approaches to design AM parts with optimal topologies and mesostructures (Ngim et al. (2007); Gaynor (2015); Zegard and Paulino (2016); Liu et al. (2018)). Surprisingly, only a limited attention has been given to optimize the in-plane material placement in AM parts that is clearly advantageous for extrusion-based technologies (Tam and Mueller (2017), Zhang et al. (2017)). Such optimization can help to capitalize the effect of in-plane anisotropy and tailor the mechanical properties in different directions to yield the best structural performance from a given component (Lopes et al. (2007); Ghiasi et al. (2010); Giorgio et al. (2020)).

The concept of varying the in-plane material orientations to reach a superior structural performance has been well explored for laminated fiber-reinforced composites (FRC). Hyer and Charette (1991) were among the first to demonstrate that the point-wise variation of the fiber paths reaches superior structural performance. Their approach involved discretizing a structure into finite elements (FE) and using the material orientation in each FE as a design variable. The result is a material orientation map that must be post-processed into a set of manufacturable fiber path trajectories. Many works were inspired by this approach, including Duvaut et al. (2000), Stegmann and Lund (2005), Huang and Haftka (2005), Legrand et al. (2006), Malakhov and Polilov (2016), Kiyono et al. (2017), etc. In another popular design approach, the fiber paths are represented as curvilinear functions, and their coefficients

4

become the design variables. Such a concept was first introduced by Nagendra et al. (1995) using Non-Uniform Rational B-Splines and was later extended to linearly varying fiber angles (Tatting et al. (2002); Lopes et al. (2008)), Bezier curves (Kim et al. (2012)), B-Splines (Honda et al. (2009); Honda and Narita (2012)), Lagrange polynomials (Wu et al. (2012)) etc. The main advantage of this method is the reduced number of design variables and the continuity of the fiber paths designed. Besides, multi-level methods have been also been proposed, in which the composite design problem is split into sub-problems to deal with the non-convex relations between fiber orientations and the physical responses in the optimization problem (Izzi et al. (2021)). At the macroscopic scale, the anisotropic response is described using lamination (Setoodeh et al. (2009)) or polar parameters (Catapano et al. (2015); Montemurro and Catapano (2017)), and the determination of optimal stacking sequence is done at the second stage.

The above techniques have been applied to multiple fiber-path optimization problems involving compliance (Stegmann and Lund (2005); Kiyono et al. (2017)), buckling loads (Wu et al. (2012)), fundamental frequency (Blom et al. (2008)), failure criteria (Lopes et al. (2008)), stress concentration (Malakhov and Polilov (2016)) etc., using both gradient-based (Stegmann and Lund (2005); Blom et al. (2008); Lemaire et al. (2015)) and evolutionary (Legrand et al. (2006); Wu et al. (2012); Huang et al. (2016)) optimization algorithms. Nevertheless, most of the works overlooked the manufacturability of the designs (Lozano et al. (2018)), thus, making it challenging to transform the optimized designs into a finished product. For detailed reviews on the design of laminated composites, the reader is referred to Ghiasi et al.

5

(2009) and Ghiasi et al. (2010).

To the authors' best knowledge, only a few works sought optimized material deposition paths to improve the structural performance in AM parts. Hoglund and Smith (2016) computed the preferred fibre angles to minimize the compliance of FFF parts and printed the optimal designs using the contour-parallel deposition strategy that approximated the local orientations. Yamanaka et al. (2016) used the analogy between the fiber paths and streamlines to find the optimal non-intersecting fiber paths that maximized the fracture strength of a 3D-printed continuous-fiber composite plate. Liu and Yu (2017) used a level-set-based method for optimizing the deposition paths in both fixed and flexible geometries (subject to topology changes), which was later extended by Liu and To (2017) to three-dimensional structures, including support constraints. Then, Roberge and Norato (2018) optimized the material orientation and spacing for maximizing the stiffness of curvilinear scaffolds produced using Direct Ink Writing (an extrusion-based AM method). Finally, Hou et al. (2021) used the stress gradients to optimize the fiber direction in a 3D-printed composite for improving the component ultimate strength. All the above methods focused on specific cases or required non-trivial post-processing steps that caused a loss of conformity between the design solutions and the printed parts, leading to a perfectible compromise. Recently, Fernandez et al. (2019) proposed a method to lift this limitation by directly enforcing the manufacturing constraints in the optimization to obtain production-ready design solutions.

The present work also imposes a set of manufacturing constraints (e.g., filament spacing and overlap control) to design optimized readily-printable

filament paths for FFF structures, with the following new contributions with respect to the state-of-the-art: (i) the proposition of a new realistic material model incorporating the phenomenological stiffness decrease before inter-filament fusion that is shown to impact the resulting optimized filament patterns significantly, and (ii) the critical comparison between a global metaheuristic algorithm and a two-step gradient-based algorithm in terms of the computational performance and the resulting optimized structural compliance.

The contribution is organized as follows: Section 2 sets up the filament path optimization problem to be solved, expressing the fundamental filament path quantities and manufacturing constraints in terms of the design variables. Then, Section 3 develops a new material model accounting for the inter-filament gaps in an FFF layer. Section 4 presents the two different approaches for optimizing the filament paths, depicting the developed algorithmic framework. Section 5 applies the methodology to a series of example structures, and finally, Section 6 lists the main conclusions, providing insights on future works.

2. Formulation of the optimization problem

The filament trajectories on an FFF layer are represented as the contours or level-sets of a B-Surface defined over the layer (Fernandez et al. (2019)). The optimized filament trajectories can be then found as the solution to a minimization problem in which the shape parameters of the B-Surface are treated as the design variables. As mentioned in the literature survey, prior works have used B-splines to represent the fiber paths. For

7

example, Honda et al. (2009) and Honda and Narita (2012) represented the fiber paths as single-valued spline functions, and Montemurro and Catapano (2017) described the distribution of fiber angles over a laminate using uniform B-surface. However, the advantage of the proposed approach is that we treat the filament paths as contours and enable a simultaneous control over both the filament angle and the spacing, thus, facilitating an easy conversion of the designs into G-code for printing. The series of steps, inspired from Fernandez et al. (2019), leading up to the formulation of the minimization problem, is presented first for the sake of completeness.

2.1. Filament path parametrization

The filament angle and spacing that describe the local filament path are formulated in terms of the contours of a B-Surface; they become continuous functions of the shape parameters of the B-Surface.

Let us assume a generic FFF component to optimize the filament paths and minimize its compliance (i.e., maximize its stiffness). The assumed component has layers of filaments printed on the $\mathbf{e_1}$-$\mathbf{e_2}$ plane and stacked in the $\mathbf{e_3}$ direction. Each extruded filament has a constant width w and a height h, as shown in Figure 1. The entire FFF component occupies a domain λ in three dimensional space that is sliced into individual domains λ_1, λ_2, $...\lambda_n$ representing the layers of the component. Under suitable assumptions on the component (cross-sections symmetrical to the mid-plane, loads non-varying along the $\mathbf{e_3}$, dimension in $\mathbf{e_3}$ smaller than along the other directions), we focus our analysis on a 2D domain Ω that represents the component mid-plane having superposed filament trajectories from layers $\lambda_{i=1,2..n}$ (Figure 1).
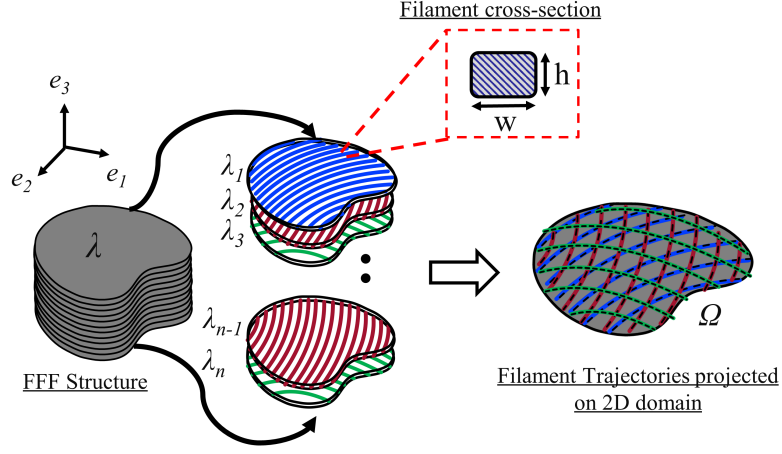
Figure 1: Two-dimensional assumption for FFF part. $\boldsymbol{\lambda}$ is composed of individual layers $\lambda_1, \lambda_2..\lambda_n$ having filaments of width w and height h. An equivalent 2D domain Ω is defined with filament trajectories from $\lambda_1, \lambda_2..\lambda_n$ projected on to it.

An ith in-plane filament layout on Ω can be described as the contours of a scalar function $\phi_i(x, y)$ defined over Ω (Honda and Narita (2011); Huang et al. (2016))

$$C_i^k = \{\mathbf{x} \mid \phi_i(\mathbf{x}) = k\ b\},\ k \in \mathbb{Z},\ \ b \in \mathbb{R},\ \mathbf{x} = (x, y) \in \Omega, \tag{1}$$

where each contour in the set C_i^k, resulting from $\phi_i = 1b, 2b...kb$, represents a single trajectory in the ith filament layout on Ω (Figure 2). Further, we also assume $b = w$, the rationale behind which will be clarified in the next section, where manufacturing constraints are imposed.

Since the contours of ϕ represent filament trajectories, it follows that the local filament angle and the spacing can also be derived from the contours of ϕ. At any point $\mathbf{x} \in \Omega$, the filament angle $\alpha_i(\mathbf{x})$ is the angle between the tangent $\mathbf{t}(\mathbf{x})$ to the contour and the $\mathbf{e_1}$ axis (shown in Figure 2). Therefore,

$\alpha_i(\mathbf{x})$ is expressed as

$$\alpha_i(\mathbf{x}) = tan^{-1}\left(\frac{-\phi_{i,x}}{\phi_{i,y}}\right), \tag{2}$$

where $\phi_{i,x}$ and $\phi_{i,y}$ are partial derivatives of the ϕ_i with respect to x and y, respectively (Honda and Narita (2011); Huang et al. (2016)). In a similar fashion, the filament spacing $l_i(\mathbf{x})$ is also denoted using the contours of ϕ_i. As Figure 2 illustrates, the filament spacing $l_i(\mathbf{x})$ is the sum of the distances from $\mathbf{x}$ to the two closest points in the adjacent contours, where $\Delta\mathbf{x}_k$ and $\Delta\mathbf{x}_{k\text{-}1}$ are correspondingly the distances from $\mathbf{x}$ to the closest points $\mathbf{x}_k^*$ and $\mathbf{x}_{k\text{-}1}^*$ in the two adjacent contours C_i^k and C_i^{k-1}. Thus, we relate the spacing $l_i(\mathbf{x})$ to ϕ_i as given below (refer to Fernandez et al. (2019) for derivation):

$$l_i(\mathbf{x}) \approx \frac{b}{|\nabla\phi_i(\mathbf{x})|}. \tag{3}$$

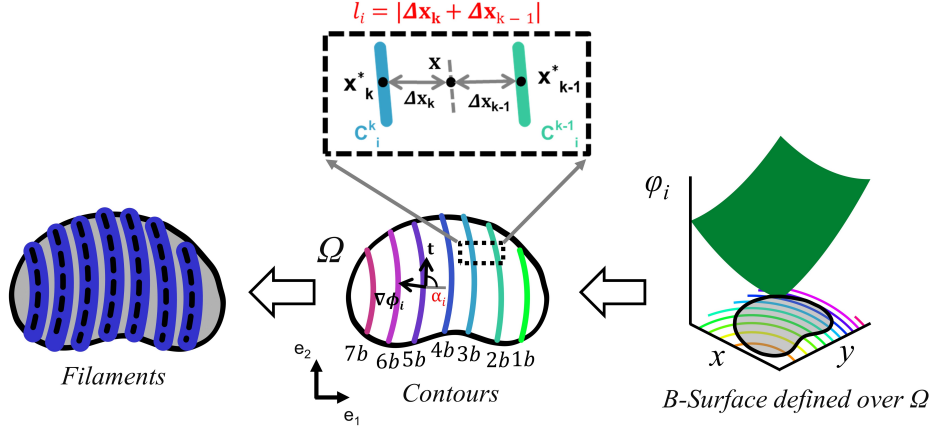Figure 2: In-plane filament trajectories represented using contours of a B-Surface. α_i : filament angle; l_i : filament spacing; $\mathbf{x}_k^*$: closest point in contour C_i^k from $\mathbf{x}$; $\mathbf{x}_{k\text{-}1}^*$: closest point in contour C_i^{k-1} from $\mathbf{x}$.

Any B-Surface is composed of individual entities called patches, the shapes

of which are influenced by a set of control points as shown in Figure 3. Assuming that the contours of a uniform bicubic B-Surface (with equidistant knots) represent the filament trajectories, we use the following set of equations to define a single patch of B-surface (Bartels et al. (1995), Marschner and Shirley (2015)):

$$x(\mathbf{\Xi}) = \mathbf{N}(\mathbf{\Xi})^{\mathbf{T}}\mathbf{X_L}; \; y(\mathbf{\Xi}) = \mathbf{N}(\mathbf{\Xi})^{\mathbf{T}}\mathbf{Y_L}; \; \phi_i(\mathbf{\Xi}) = \mathbf{N}(\mathbf{\Xi})^{\mathbf{T}}\mathbf{d_L}, \qquad (4)$$

where $\mathbf{N}(\mathbf{\Xi})$ is the vector of uniform bicubic basis functions, the symbol $\mathbf{\Xi} = (\xi, \eta)$ represents the coordinates of the patch in parent space, while $\mathbf{X_L}$, $\mathbf{Y_L}$ and $\mathbf{d_L}$ denote the vectors comprising the 3D positions of a grid of control points that surround the patch in physical space (see Figure 3).

Eq. (4) relates ϕ_i to the local control point heights $\mathbf{d_L}$, therefore enabling the contours of ϕ_i, and in turn, the filament path angle α_i (Eq. (2)) and spacing l_i (Eq. (3)) to be controlled using them. Thus, if 'n' sets of filament trajectories are represented using 'n' number of B-Surfaces, then the entries of the entire vector of control point heights of the B-Surfaces $\mathbf{d} = \{\mathbf{d_1}, \mathbf{d_2}, ...\mathbf{d_n}\}$ become the design variables for the filament trajectories in the FFF structure. The total number of design variables (N_{dv}) is determined from the number of B-surface patches as given below:

$$N_{dv} = n \; CP_x \; CP_y = n(P_x + 3)(P_y + 3), \qquad (5)$$

where CP_x and CP_y denote the number of control points used per B-Surface in $\mathbf{e_1}$ and $\mathbf{e_2}$ directions, with P_x and P_y being the corresponding patch number in each direction. For example, Figure 3 employs a total of $N_{dv} = 42$ design variables in a single layer ($n = 1$).
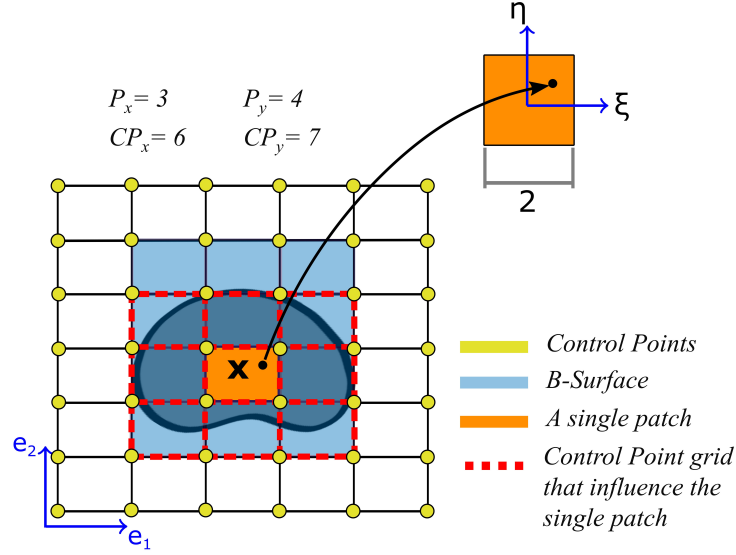
Figure 3: Patches of a uniform bicubic B-Surface defined over a layer. P_x : Number of patches along $\mathbf{e_1}$; P_y : Number of patches along $\mathbf{e_2}$; $CP_x = P_x + 3$: Number of control points along $\mathbf{e_1}$; $CP_y = P_y + 3$: Number of control points along $\mathbf{e_2}$.
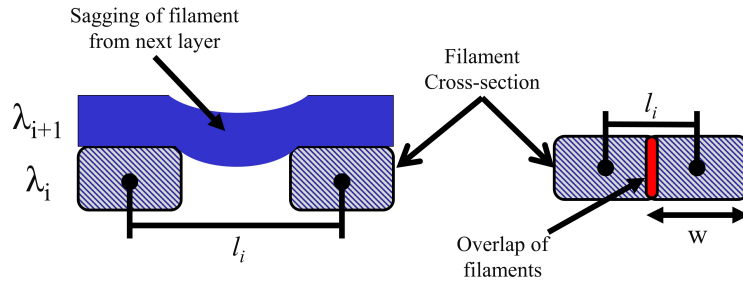
2.2. Imposing manufacturing constraints

Figure 4: Manufacturing filament spacing constraint; sag and overlap, respectively, define the maximum and minimum filament spacing

Production-ready solutions can be yielded from design optimization, provided proper manufacturing constraints are incorporated in the optimization

process. For instance, in the case of laminated composites, the fiber paths are often constrained not to undergo large curvatures due to the limitations in the Automated Fiber Placement (AFP) technique (Lemaire et al. (2015); Huang et al. (2016)). Here, the two essential constraints of the FFF process are considered (refer to Figure 4): (i) the *no-overlap* constraint between neighbouring filaments, i.e., the path spacing l_i is set larger than or equal to the filament width ($l_i \geq w$) and (ii) the *no-sag* constraint that states that any two adjacent filaments cannot be spaced larger than a prescribed value of l_{max} ($l_i < l_{max}$) to avoid sagging of the filaments deposited on the previous layer, where l_{max} is a parameter chosen based on the printer capabilities to bridge two unsupported points.

The aforementioned manufacturing constraints are equivalently expressed as constraints on the gradient of ϕ_i for relating them to the design variables. With the assumption $b=w$ introduced in Section 2.1, the expressions for no-overlap and no-sag constraints are derived from Eq. (3) and stated as follows, respectively:

$$|\nabla \phi_i| \leq 1 \tag{6}$$

$$|\nabla \phi_i| \geq \frac{b}{l_{max}} \tag{7}$$

It is emphasized that Eqs. (6) and (7) express *local* constraints, which must be respected at every point in a layer λ_i. Due to the practical challenges in implementing the local constraints (Amstutz (2010); Amstutz and Novotny (2010); Amstutz et al. (2012)), they are correspondingly transformed into

the following integral expressions (Le et al. (2010); Fernandez et al. (2019)):

$$G_i^a = \int_\Omega S_t(|\nabla \phi_i|^2 - 1)d\Omega \leq 0 \tag{8}$$

$$G_i^b = \int_\Omega S_t\left(1 - \left(|\nabla \phi_i|\frac{l_{max}}{b}\right)^2\right)d\Omega \leq 0, \tag{9}$$

where the step function S_t is introduced to facilitate the constraint enforcement through penalty methods (explained in next section). Thus, we set:

$$S_t(\Theta) = \begin{cases} 0, & \text{if } \Theta \leq 0 \\ 1, & \text{if } \Theta > 0 \end{cases} \tag{10}$$

2.3. The minimization problem

Having expressed the printing trajectories and manufacturing constraints in terms of the contours of B-surfaces, the optimization problem can now be defined. The objective is to find the optimal control point heights of the B-Surfaces that minimize the compliance of Ω, subject to no-overlap (G_i^a) and no-sag (G_i^b) constraint. The corresponding mathematical formulation is given as

$$\underset{\mathbf{d_1},\mathbf{d_2}..\mathbf{d_n}}{\text{minimize}} \quad \text{compliance (c)}, \tag{11}$$

$$\text{subject to:} \quad G_i^a \leq 0, \quad i = 1, 2, ..n$$

$$G_i^b \leq 0, \quad i = 1, 2, ..n,$$

where the objective/cost function to be minimized is the compliance $c = \int_\Omega \boldsymbol{\sigma} : \boldsymbol{\epsilon} \, d\Omega$ (twice the strain energy) computed from the Cauchy stress tensor $\boldsymbol{\sigma}$ and the infinitesimal strain tensor $\boldsymbol{\epsilon}$ using finite element analysis (Brampton et al. (2015); Esposito et al. (2019)) .

The above minimization problem is recast into the following unconstrained minimization problem using the penalty method (Nocedal and Wright (2006);

14

Price et al. (2006); Ali and Zhu (2013)):

$$\underset{\mathbf{d_1,d_2,..d_n}}{\text{minimize}} \quad c \; + \; \epsilon_p \Bigg(\sum_{i=1,2,..n} (G_i^a)^2 + (G_i^b)^2 \Bigg), \tag{12}$$

where the quadratic function $p = c + \epsilon_p \, ((G_{i=1..n}^a)^2 + (G_{i=1..n}^b)^2)$ becomes the new *penalized cost function* to be minimized, and $\epsilon_p \, (> 0)$ is the penalty coefficient that penalizes the new cost function proportional to the constraint violations. Penalty methods offer the simplest approach to enforce the constraints in a minimization problem. But an informed choice of the penalty coefficient is crucial, as over-penalizing or under-penalizing the constraints may hinder the minimization algorithm from finding the actual minimum.

3. Anisotropic material model accounting for the effect of inter-filament spacing

The mechanical performance of FFF parts relies upon a multitude of FFF parameters: filament angle, build orientation, infill density, printed material, extrusion temperature, nozzle diameter, bed temperature etc., among which, the filament angle and density are widely recognized to play dominant roles (Fayazbakhsh et al. (2019); Cuan-Urquizo et al. (2019)). A noteworthy highlight of this work is, in fact, a new material model that predicts the component response accounting for the local filament angle and density.

When satisfying simplifying assumptions, anisotropic heterogeneous materials like composites have been popularly modelled using homogenization approaches (Kalamkarov et al. (2009)). However, homogenizing a freely deposited FFF part would be questionable from a theoretical viewpoint since the principles of scale separation and periodicity would be generally invalid.

Therefore, the present work computes the stiffness components based on the mesostructural data (i.e., filament angle and spacing) in the finite element model without assuming full scale separation. With a sufficiently refined mesh, this approach works in smaller material regions and leads to even more accurate results. For this purpose, we extend the classical approach of Fernandez et al. (2019), in which a transversely isotropic elasticity tensor is rotated by the local filament angle $\alpha_i(\mathbf{x})$ and linearly scaled by the local density/volume-ratio $\nu_i(\mathbf{x})$, where the *volume ratio*, expressed below, is the amount of filament material in a $l_i \times l_i \times h$ Representative Volume Element (Figure 5).

$$\nu_i(\mathbf{x}) = \frac{l_i b h}{l_i^2 h} \approx |\nabla \phi_i(\mathbf{x})| \qquad (13)$$
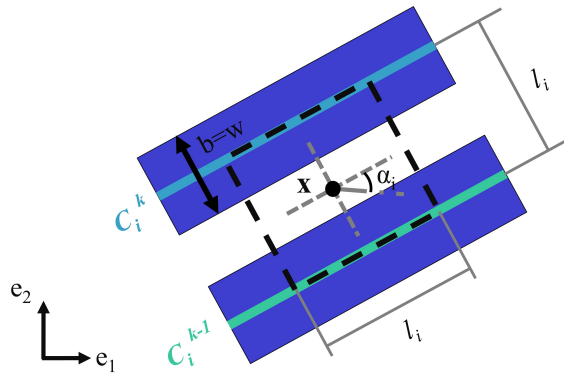

Figure 5: Definition of volume ratio. ν_i is the ratio of filament material in the $l_i \times l_i \times h$ Representative Volume Element.

The simplified technique to linearly scale all the stiffness components with the volume ratio assumes significant transverse stiffness before inter-filament fusion, thereby ignoring the filament bonding mechanism and leading to less realistic printing patterns (will be shown in Section 5). Thus, to avoid such

solutions, a material model incorporating the effect of inter-filament spacing is developed below.

Let $\Psi_i(\mathbf{x})$ denote the strain energy density due to the ith filament layout. Then, the strain energy density $\Psi(\mathbf{x})$ for the whole FFF part is the sum of individual contributions from the strain energy densities due to n filament layouts on Ω (from λ_1, $\lambda_2...\lambda_n$), i.e.,

$$\Psi(\mathbf{x}) = \Psi_1(\mathbf{x}) + \Psi_2(\mathbf{x}) + ..\Psi_n(\mathbf{x}) \tag{14}$$

Taking the assumptions of linear elasticity and small-strains, and recalling $\boldsymbol{\sigma} = \partial\Psi/\partial\boldsymbol{\epsilon}$, the strain energy density $\Psi_i(\mathbf{x})$ is expressed as a quadratic function of the strain tensor $\boldsymbol{\epsilon}$

$$\Psi_i(\mathbf{x}) = \frac{1}{2}\,\boldsymbol{\epsilon}(\mathbf{x}) : \mathbf{C}_i^*(\mathbf{x}) : \boldsymbol{\epsilon}(\mathbf{x}), \tag{15}$$

where the elasticity tensor $\mathbf{C}_i^*(\mathbf{x})$ at a point $\mathbf{x} \in \Omega$ is a function of the filament angle α_i and the volume-ratio ν_i at that point, i.e., $\mathbf{C}_i^*(\alpha_i(\mathbf{x}), \nu_i(\mathbf{x}))$.

If transverse isotropy is assumed in layer λ_i, then the elasticity tensor $\mathbf{C}_i^*(\mathbf{x})$ has five independent components in a local coordinate system: s_{11}, s_{22}, s_{12}, s_{44} and s_{23}, where the adopted indices are consistent with the Voigt notation (Kollar and Springer (2003)). The goal is to represent that the stiffness component along the filament direction s_{11} dominates if adjacent filaments do not touch each other, i.e., for low values of volume ratio ν_i. The other components s_{22}, s_{12}, s_{44} and s_{23} come into play only when the inter-filament bonding occurs, i.e., when a given minimum threshold of ν_i has been reached. Modelling this behaviour implies that the printing and the transverse direction stiffness are treated differently with respect to ν_i, (a decoupled behaviour).

17

Figure 6 sketches the assumed evolution of the five stiffness components as functions of the volume ratio. The stiffness along the filament extrusion direction s_{11} is modelled as a linear function of ν_i as follows:

$$s_{11}(\nu_i) = c_{11}\nu_i, \tag{16}$$

where c_{11} is the stiffness component along the filament direction at full volume ratio (i.e. corresponding to a volume filled at 100% by the filament material).
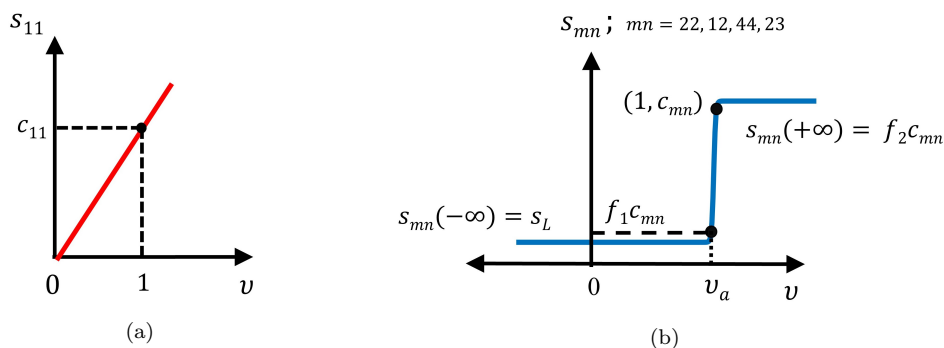

Figure 6: Stiffness variation as function of the volume-ratio. (a) s_{11} is linear function of ν. (b) The components $s_{22}, s_{12}, s_{44}, s_{23}$ are hyperbolic tangent functions of ν. Only s_{11} is significant before inter-filament fusion. The other components are very low for $\nu \leq \nu_a$ and reach a saturated state once the filaments are completely fused.

On the other hand, the components s_{22}, s_{12}, s_{44} and s_{23} are almost zero for widely spaced adjacent filaments. When the filaments start to bond with each other, the four stiffness components rapidly rise and subsequently reach a saturated maximum value once the filaments are completely fused. Figure 6b shows a hyperbolic tangent curve that is assumed to model this behaviour. Accordingly we state:

$$s_{mn}(\nu_i) = a_3 \tanh(a_1\nu_i + a_2) + a_4, \tag{17}$$

18

where $tanh(z) = (e^z - e^{-z})/(e^z + e^{-z})$, and s_{mn} corresponds to each of the four stiffness components s_{22}, s_{12}, s_{44} and s_{23}, for which the unknown constants a_1, a_2, a_3 and a_4 must be individually determined.

To compute the unknown constants in Eq. (17), we solve the following system of equations that result from the conditions at $\nu_i = \nu^l$, ν^a, 1 and ν^u:

$$s_{mn}(\nu^l) = s_L \tag{18a}$$

$$s_{mn}(\nu^a) = f_1 c_{mn} \tag{18b}$$

$$s_{mn}(1) = c_{mn} \tag{18c}$$

$$s_{mn}(\nu^u) = f_2 c_{mn}, \tag{18d}$$

where ν^l and ν^u, respectively, denote the lower and upper limits of the volume ratio ν_i in a layer. In a physical sense, ν^l is equal to zero, and ν^u can be slightly more than one, provided a meagre percentage of inter-filament overlap is allowed. However, assuming that a saturated state already exists at volume ratios ν^l and ν^u, both quantities are set to $-\infty$ and $+\infty$, respectively, for the analytical solution of Eq. (18). The volume ratio ν^a denotes the *activation point* at which the inter-filament bonding is assumed to start. Accordingly, ν_a must be chosen close to one ($\nu_a \to 1$) for a realistic inclusion of the filament spacing effect. The parameter s_L denotes a very small user-defined value for the four stiffness components when the filaments are widely spaced (at $\nu_i = \nu^l$), whereas c_{mn} denote their values when the filaments are fused, i.e., at 100% volume ratio ($\nu_i = 1$). Finally, the quantities f_1 and f_2 are the user-defined fractional constants that scale the stiffness c_{mn} at $\nu_i = 1$ and assign them at ν^a and $\nu_i = \nu^u$, respectively.

Note that, for simplicity, the values of c_{mn} are taken from an inherently

transversely isotropic material such as unidirectional fiber-reinforced composite. This is because, unlike the parts produced from subtractive or formative methods, the properties of the bulk material do not necessarily translate to the final FFF parts. Since the characteristics of FFF components are the result of numerous design and process parameters, an experimental characterisation of the components, including these parameters, would be necessary to determine their material constants.

After determining all the unknown constants in Eq. (17), the transverse isotropic elasticity tensor is assembled in the local coordinate system and rotated by the filament angle $\alpha_i(\mathbf{x})$ to find the final elasticity tensor $\mathbf{C}_i^*(\mathbf{x})$.

Considering how the role of inter-filament spacing has been incorporated here, it seems natural that the manufacturing constraints might also be embedded into this material model. However, it is not straightforward to define the stiffness components' evolution with artificial bounds dictated by the manufacturing constraints. This explains why manufacturing constraints are separately imposed using the penalty formulation.

4. Solution methodologies

The minimization problem in Eq. (12) is solved using two methods: (i) a two-step gradient-based minimization, and (ii) Differential Evolution (Storn and Price (1995, 1997); Price et al. (2006)).

In general, gradient-based methods start the minimization process from a single point and iteratively proceeds to better approximations along directions computed from the gradient of the objective function at each point. Although gradient-based methods ensure fast convergence to minimum solu-

tions, they are sensitive to the starting point, and may converge to a local minimum if close-to-zero gradients are encountered in the process. In order to drive the gradient-based methods towards the global optimum, a two-step approach is set up here, following Fernandez et al. (2019). Within the two-step gradient-based minimization, first an initial optimized design with straight and parallel toolpaths having uniform orientations $\alpha_{i=1,2..n}^{\text{in}}$ is obtained. Then, the control point heights $\mathbf{d_i^{in}}$ corresponding to the uniform orientations α^{in} are supplied as the starting point to solve the curvilinear filament optimization in Eq.(12). The initial control point heights $\mathbf{d_i^{in}}$ for the optimization are calculated using the following relation:

$$\mathbf{d_i^{in}} = [-\sin(\alpha_i^{\text{in}})\mathbf{X}, \cos(\alpha_i^{\text{in}})\mathbf{Y}]^{\text{T}}, \tag{19}$$

where $\mathbf{X}$ and $\mathbf{Y}$ are the vectors of control point coordinates on $\mathbf{e}_1$-$\mathbf{e_2}$ plane. On solving the minimization problem in Eq.(12), convergence is reported at a kth step if the following criteria are satisfied:

$$||\Delta\mathbf{d_k}|| \leq 10^{-ag_1} \ \& \ ||\nabla\mathbf{p}(\mathbf{d_k})|| \leq 10^{-ag_2}, \tag{20}$$

where $\Delta\mathbf{d_k}$ indicates the difference in the vector of design variables at the kth step and previous steps, the quantity $\nabla\mathbf{p}(\mathbf{d_k})$ is the gradient of the penalized objective function p at the kth step, while ag_1 and ag_2 (*AccuracyGoal*) are positive integers that specify the convergence tolerance. Furthermore, to accelerate the convergence to optimum solutions, analytical sensitivities calculated with automatic differentiation techniques are supplied at every iteration.

Differential Evolution operates by a principle that is agnostic to the gradient of the objective function. It is a population-based metaheuristic al-

gorithm that applies evolutionary principles (mutation, recombination and selection) to a randomly initialized population of candidate solutions of size SP (search points) and probes the function landscape for the minimum solution. During the process, the scale factor $F \in [0, 2]$ (Gämperle et al. (2002)) determines the perturbation size to generate new candidate solutions from the existing ones, whereas the diversity (distribution over the function space) between them is controlled by Crossover-Probability $C_r \in [0, 1]$. C_r close to one favours exploitation of already found good points to look for better points in their vicinity (Sá et al. (2008)). On the other hand, a C_r close to zero explores new regions of the design space to maximise the probability of finding the global minimum[1]. The search for the minimum solution continues until the preset maximum number of generations (G_{max}) is reached or if the difference between the best function values in the new and old populations, as well as the distance between the new best point and the old best point, are less than a tolerance of 10^{-ag}, with ag being a user-set positive integer (Brett Champion (2008)). Differential Evolution is prone to find the global minimum of complex functions without getting trapped at local solutions. However, working with a population of solutions, Differential Evolution incurs higher computational cost and is highly reliant on the control parameters (SP, C_r and F), the manual tuning of which is a tedious task.

Both Differential Evolution and the two-step gradient based minimization are applied for filament path optimization in Section 5 and are comparatively evaluated in terms of solution quality, computational cost and operational

---

[1]The 0-1 scale of C_r mentioned here is reversed to the classical Differential Evolution proposed by Storn and Price (1995) (Oleksandr (2016))
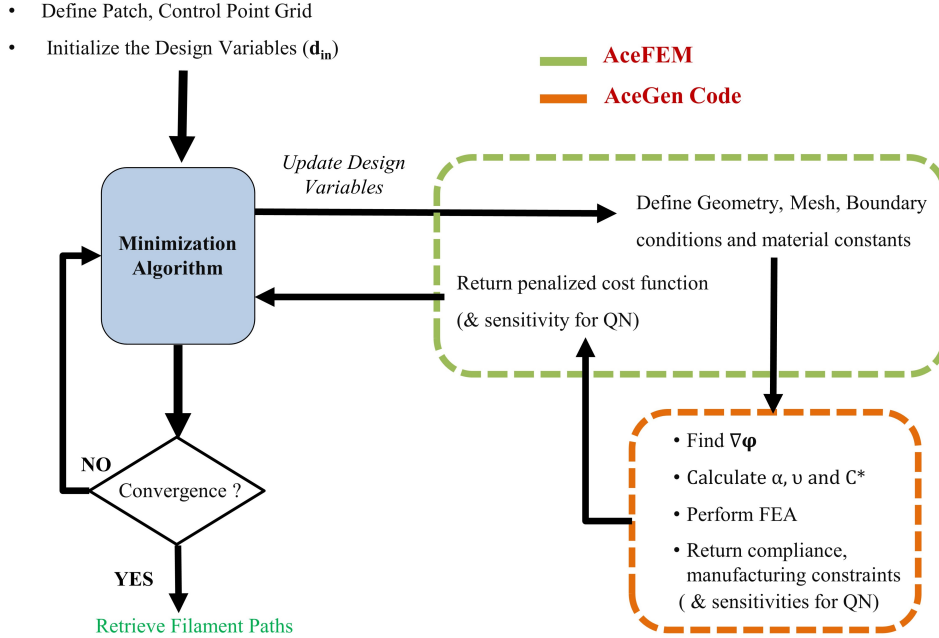
22

difficulties.

Figure 7: Developed optimization framework in Mathematica, AceGen and AceFEM. AceGen is used to develop FE codes, while AceFEM is used for preprocessing and post-processing tasks.

The workflow of the entire framework developed in Mathematica summarizing each step is depicted in Figure 7. While Differential Evolution is already available as Mathematica's built-in minimiser, the two-step gradient based minimization is implemented using the Quasi-Newton algorithm in Mathematica. To evaluate the structural performance, the finite element procedures are implemented using specialized packages called AceGen and AceFEM (Korelc (2007)). In AceGen, the coding can be efficiently done in a symbolic form to automatically derive the complex formulae needed in numerical analysis. On the other hand, the AceFEM package is a general

finite element environment that is designed to perform preprocessing and post-processing steps of finite element analysis.

5. Application to two-dimensional structures

We apply the described methodology to optimize the filament paths of 2D structures in three separate sections. Section 5.1 makes a comparative assessment of the two-step gradient-based minimization and the Differential Evolution. Section 5.2 evaluates the benefits of optimized filament paths against the standard straight filament patterns. Finally, Section 5.3 compares the proposed material model with the model of Fernandez et al. (2019) to investigate the effect of decoupling the printing and transverse stiffness components.

5.1. Two-step gradient-based minimization-Vs-Differential Evolution

Prior to comparing the minimization approaches, we first study the influence of essential parameters like number of patches (P_x, P_y), FE mesh and penalty coefficient on the optimization process. Based on the insights on these user-parameters, the subsequent steps assume suitable values for the parameters to apply and compare both minimization approaches.

The entire section employs an MBB (Messerschmitt-Bölkow-Blohm) beam to optimize the filament paths. The corresponding geometry, boundary conditions, and an example patch arrangement for the optimization are given in Figure 8. Note that arbitrary load magnitudes have been assumed for the structure, as the applied magnitude does not influence the optimized solutions under linear elasticity assumptions. A total thickness of $t = 1$ mm, a filament width of $w = 0.6$ mm and a maximum allowable gap of l_{max}=1.6

24

mm are assumed (as in Fernandez et al. (2019)). At full-volume fraction, the material properties are taken to be: $c_{11} = 152.47$ GPa, $c_{22} = 15.44$ GPa, $c_{12} = 7.46$ GPa, $c_{44} = 4.550$ GPa and $c_{23} = 9.410$ GPa (Kollar and Springer (2003)), along with the following material model parameters: $\nu^a = 0.9$, $s_L = 10^{-4}$ GPa, $f_1 = 10^{-3}$ and $f_2 \approx 1.03$ to 1.1.
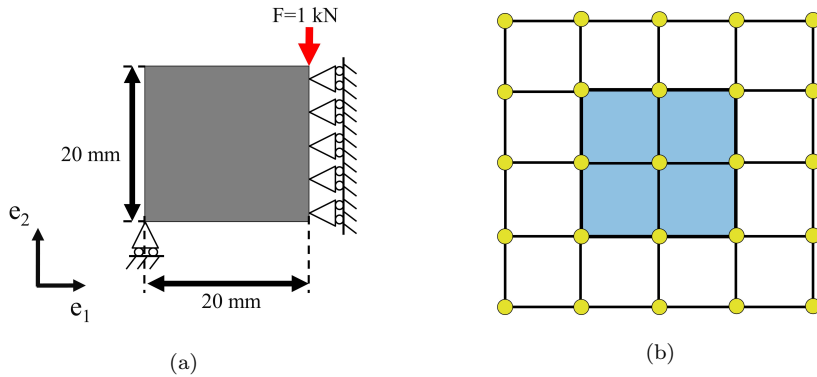

Figure 8: MBB structure and patch arrangement. (a) Geometry of MBB structure assuming symmetric boundary conditions along the midside vertical axis and a load of F = 1kN, (b) Patch arrangement with $P_x = 2$, $P_y = 2$ yields $N_{dv} = 50$ for $n = 2$.

Parametric study on patch number, FE mesh and penalty coefficient

Two parametric studies are conducted while optimizing the MBB structure: (i) the roles of the B-surface patch number and the penalty coefficient are investigated simultaneously for a given FE mesh, and (ii) the effect of refining the FE mesh is examined, keeping the number of patches constant. For simplicity, both studies are conducted using two-step gradient based minimization, assuming a single layer and imposing only the no-overlap condition. A tolerance $ag_1=2/ag_2=2$ is assumed since convergence criterion is not satisfied for stricter tolerance.

25

The first parametric study uses a 32-by-32 bilinear FE mesh and conducts the filament path optimization for four different patch arrangements P_x-by-P_y: 1-by-1, 2-by-2, 3-by-3 and 4-by-4. The corresponding initial design variables $\mathbf{d^{in}}$ are computed from $\alpha^{in} = 70.59°$ and the minimization problem in Eq. (12) is solved for a range of penalty coefficients ϵ_p. Starting from the highest possible value, the penalty coefficient is reduced ensuring that the overlap $ol = w - l_i$ in the optimum solution stays within a reasonable limit, for example, $ol \leq 10\%$ of w.

For the assumed patch numbers, Figure 9a depicts the maximum volume ratio ν^{max} obtained with different penalty coefficients ϵ_p. Figures 9b and 9c, respectively, depict the ratio of final compliance to the initial compliance (c_f/c_{in}) and the computational time (T) against penalty coefficients ϵ_p, while Figure 9d shows the computational time T for achieving a given value of compliance reduction c_f/c_{in}.

Figure 9a indicates a trend typical to any penalty-based optimization process. Regardless of the patch number, the decrease in the penalty-coefficient ϵ_p increases the maximum volume ratio ν^{max}, denoting the proportional degree of constraint violation (overlap) in the optimum solutions. The artificial limit set on the overlap ol dictates the lowest penalty coefficient, whereas its upper limit is due to the effect of *ill-conditioning*, inherent to the penalty methods of gradient-based approaches (Nocedal and Wright (2006)). Any attempt for a stronger constraint imposition using higher penalty coefficients than those shown in Figure 9a does not guarantee convergence and may prematurely terminate the minimization process. Therefore, suitable penalty coefficients are chosen by a trial and error approach, adopting a compromise

26

between imposing constraints to the desired extent and achieving convergence quickly, while respecting the user-defined limit on the local constraint violation (e.g., $ol \leq 10\%$ of w).
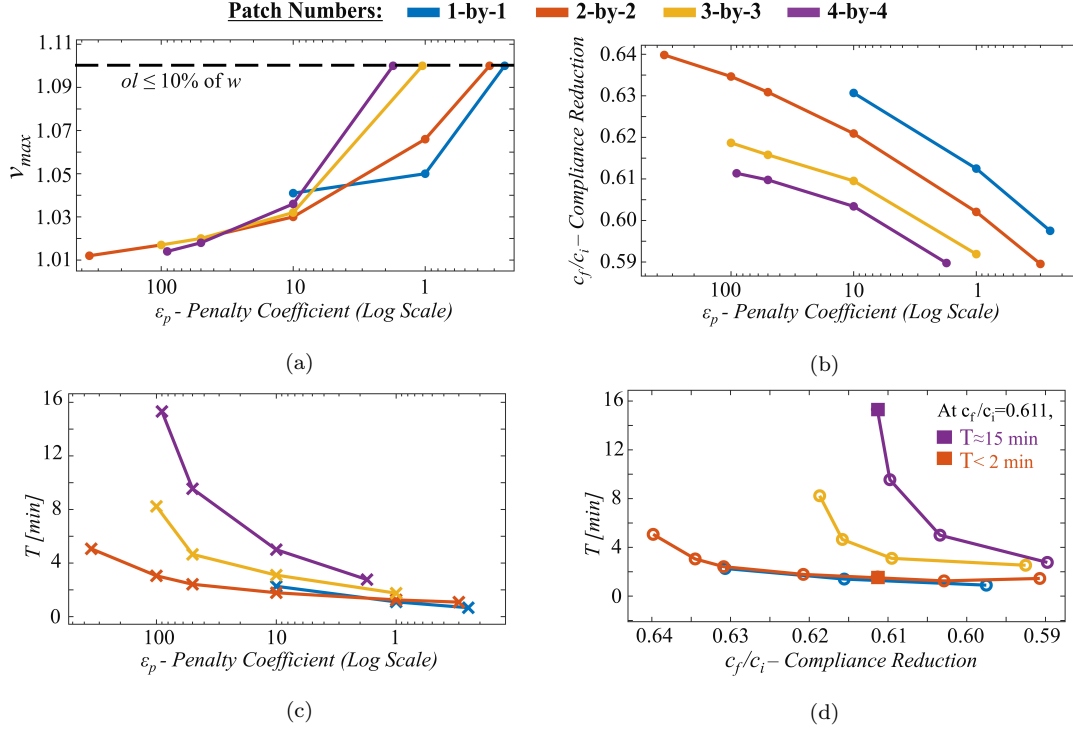

Figure 9: Parametric study on penalty coefficient and patch number. (a) Maximum volume ratio ν_{max} increases with decrease in ϵ_p. Minimization process do not converge for high penalty coefficient ϵ_p and the artificial condition, $ol \leq 10\%$ of w, sets the lower limit of ϵ_p. (b) For most ϵ_p values, a higher number of patches reaches a lower compliance reduction c_f/c_{in}. (c) Computational time T increases with the number of patches, particularly at high ϵ_p. (d) For reaching a given value of compliance reduction c_f/c_{in}, the 3-by-3 and 4-by-4 patches consumes a much higher computational time T.

Figure 9b illustrates that the higher patch numbers yield lower compliance reduction factors c_f/c_{in} for most penalty coefficients ϵ_p. Clearly, a

27

higher patch number reaches a reduced compliance by exploiting a larger design space unavailable for a lower patch number. However, the respective numerical implications must also be accounted. Figure 9c shows that the computational time T for the 3-by-3 and 4-by-4 patches significantly increase as the ϵ_p gets higher, a sign common to ill-conditioned systems. As a result, Figure 9d shows that a given compliance reduction of c_f/c_{in}=0.61 is attained by the 4-by-4 patch in $T \approx 15$ minutes, for which the 2-by-2 patch takes less than 2 minutes.

Thus, as expected, the increased design freedom of a higher patch number is achieved at a higher computational cost that increases further when constraints are enforced stricter. Deducing from these results, we can conclude that a designer can initially opt for a lower patch number; more patches can be chosen to refine the results if they appear too crude or if the further gain in stiffness is aimed.
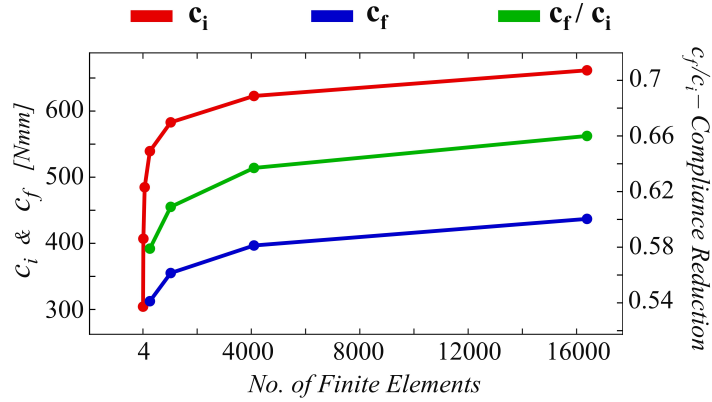

Figure 10: Parametric study on the influence of mesh size with a 2-by-2 patch arrangement. c_f and c_f/c_i increase asymptotically at higher number of finite elements. For too few finite elements, minimization process did not converge.

The second parametric study uses a 2-by-2 patch and solves the minimization problem (Eq. (12)) for a series of FE mesh, varying the element numbers as : $2^m \times 2^m$, with $m = 1, 2...7$. As previously discussed, the penalty coefficients in all cases are set through a trial and error method to maintain the same level of overlap in the final solutions and facilitate their comparison. Figure 10 plots the initial compliance c_{in}, final compliance c_f and the compliance reduction c_f/c_{in} against the number of finite elements used.

The initial compliance c_{in} in Figure 10 shows a sharp increase at the beginning that later becomes asymptotic as finite element meshes are refined. As expected, coarser meshes are stiffer and increasing the number of finite elements leads to converged meshes. Note that the final compliance c_f and the compliance reduction c_f/c_{in} follow trends similar to the initial compliance c_{in}, although both c_f and c_f/c_{in} are not plotted for low number of finite elements. The reason is that the optimisation fails to converge for too few finite elements due to the poor accuracy of the solutions from coarse meshes. Thus, a sufficient number of finite elements (at least close to converged mesh) must be employed when optimizing the filament paths to yield accurate results and enable convergence at the optimum solutions.

Based on the results presented so far, the 2-by-2 patch arrangement and 32-by-32 elements FE mesh are chosen for the comparative study of the two minimization approaches.

Two-Step gradient based minimization: filament path solutions

Now, the two-step gradient-based minimization is applied for optimizing a two-layer $(n = 2)$ MBB structure using the 2-by-2 patch and 32-by-32 FE mesh. The initial design variables corresponding to the two layers, $\mathbf{d}_1^{in}$ and

$\mathbf{d_2^{in}}$, are calculated from $\alpha_1^{in} = 61.8°$ and $\alpha_2^{in} = 14.3°$ (Eq. (19)), respectively. A penalty coefficient ϵ_p=225, which is the largest value that achieves convergence, is used to penalize constraint violations to a maximum extent. The tolerance $ag_1 = 2/ag_2 = 2$ is again assumed and the minimization problem of Eq. (12) is solved.
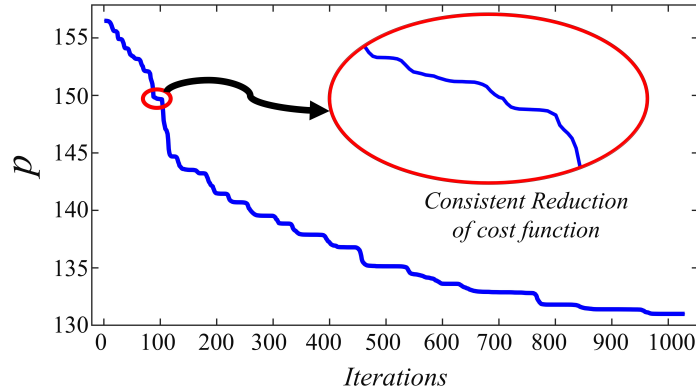

Figure 11: Convergence curve for penalized cost function. The cost function consistently reduce with each iteration.

In a AMD Ryzen 5 3400G processor (3.70 GHz and 64 GB RAM), the minimization process converged in $T = 18$ minutes with a final penalized cost function of $p_f = 130.847$. Figure 11 plots the convergence curve of the penalized cost function p. The final converged solution has a compliance c_f=130.842 Nmm and constraint quantities measuring $\epsilon_p(G_1^a)^2 = 0.002$, $\epsilon_p(G_2^a)^2 = 0.003$, $\epsilon_p(G_1^b)^2 = 0$ and $\epsilon_p(G_2^b)^2 = 0$. The results do not show any violation of the no-sag constraint, although the positive close-to-zero G_1^a and G_2^a indicate that the no-overlap constraint was meagerly violated ($ol \approx$ 1% of w). Figure 12 shows the optimized filament paths for two layers, the corresponding volume ratio plots, and the local compliance measure $c_{loc} =$

30

$\boldsymbol{\sigma} : \boldsymbol{\epsilon}$ in the structure.
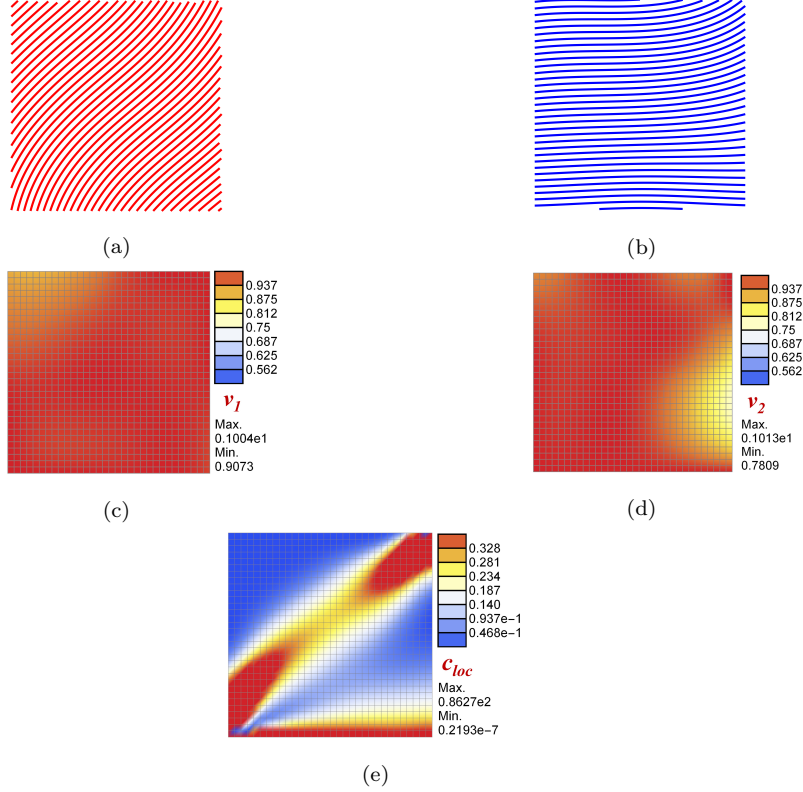

(a)

(b)

(c)

(d)

(e)

Figure 12: Optimized filament paths using two-step gradient-based approach. (a) Center-lines of optimized filaments in Layer-1, (b) Centerlines of optimized filaments in Layer-2, (c) Volume-ratio in Layer-1, (d) Volume-ratio in Layer-2, (e) Plot with a local measure of compliance ($\boldsymbol{\sigma} : \boldsymbol{\epsilon}$).

Differential Evolution: filament path solutions

Differential Evolution is applied for the filament path optimization, again using a 2-by-2 patch, a 32-by-32 mesh, and two layers ($n = 2$). For a success-ful application of the Differential Evolution, we choose the suitable values of cross-probability C_r, population size SP, and the maximum number of gen-erations G_{max} through a manual tuning process, i.e., a trial and error fashion

31

(detailed in Appendix A). The entire parameter tuning process maintains a constant scale factor of $F = 0.6$ (Gämperle et al. (2002)), a convergence tolerance of $ag \approx 7$ (a low tolerance avoids possible premature termination), and a penalty coefficient of $\epsilon_p = 10^5$. The effect of ill-conditioning does not dictate the upper limit of ϵ_p in Differential Evolution. Here, the candidate solutions enter the infeasible design space regardless of the magnitude of penalty coefficient. However, the high cost function value assigned for constraint violations solutions discourages Differential Evolution from preferring them for subsequent generations, avoiding the convergence to infeasible design space.

For comparing with the two-step gradient-based approach, the solution from the control parameters $C_r = 0.01$, $SP = 135$, $G_{max} = 3000$ is used. The corresponding penalized cost function $p_b = 136.45$, attained in $T \approx 30$ hours, is comprised of the compliance $c_b = 136.39$ Nmm and the constraint quantities $\epsilon_p (G_1^a)^2 = 0.05$, $\epsilon_p(G_1^b)^2 = 0.01$, $\epsilon_p(G_2^a)^2 = 0$ and $\epsilon_p(G_2^b)^2 = 0$. Figure 13 shows optimized filament paths from Differential Evolution, their respective volume ratio plots, and the local compliance measure c_{loc} in the structure. Additionally, Figure 13a and 13b also show the optimized filament paths from the two-step gradient based approach superposed onto the Differential Evolution solutions for comparison.
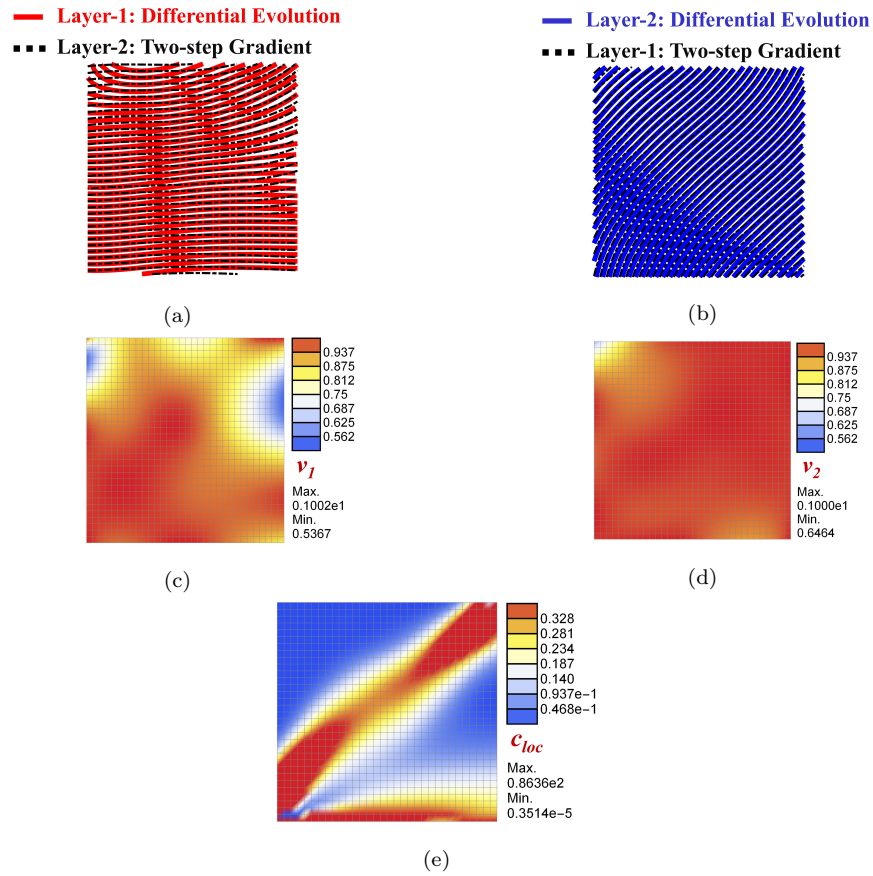
32

Figure 13: Optimized filament paths in MBB structure using Differential Evolution. (a) Centerlines of optimized filaments in Layer-1 of Differential Evolution superposed with the centerlines of optimized filaments in Layer-2 of the gradient-based method from Figure 12b, (b) Centerlines of optimized filaments in Layer-2 of Differential Evolution superposed with the centerlines of optimized filaments in Layer-1 of the gradient-based method from Figure 12a, (c) Volume-ratio in Layer-1 (d) Volume-ratio in Layer-2, (e) Plot with a local measure of compliance ($\boldsymbol{\sigma} : \boldsymbol{\epsilon}$).

Observing the results, we infer that the two-step gradient-based and Differential Evolution have attained slightly dissimilar filament patterns (compare Figures 12 and 13). The two-step gradient-based approach started from

33

an informatively chosen initial point and consistently reduced the cost function at subsequent iterations to converge at a final compliance of $c_f = 130.842$ Nmm in $T = 18$ minutes (refer to Figure 11). On the other hand, Differential Evolution employed many candidate solutions and searched the function space for the minimum solution, retaining the best candidate solution it encountered throughout the search process (hence the staircase effect in Figure A.23). At the end of 3000 generations completed in $T \approx 30$ hours ($=$ 1800 minutes), the best candidate solution from Differential Evolution had a compliance of $c_b = 136.39$ Nmm. A critical comparison is next performed considering different aspects of the utilized methodologies.

(i) Efficiency: In problems where several local minima are assumed, population-based methods such as Differential Evolution may be frequently preferred over gradient based methods, despite their high computational cost. However, in the present work, the two-step gradient-based minimization could produce an acceptable solution by reaching a final compliance very near to the Differential Evolution $((c_b\text{-}c_f)/c_f \times 100 = 4.2\%)$ at a much lower computational cost. (ii) *Operational Difficulties:* Although Differential Evolution is simple to implement, the need to tune the control parameters for each problem makes Differential Evolution challenging to operate. (iii) *Influence of ν^a:* Finally, Differential Evolution should be avoided because it struggles with the proposed material model. Activation points ν_a larger than 0.9 often randomly terminated the Differential Evolution due to an ill-conditioned stiffness-matrix in the FE procedure. This is further discussed in section 5.3, where the influence of the material parameter ν^a is studied.

For the reasons mentioned above, the two-step gradient based minimiza-

tion will be applied to the filament path optimization in the remainder of this contribution.

5.2. Optimized curved filament pattern-Vs-standard straight filament patterns

This section compares the structural compliance of optimized filament patterns against the commonly used 45°/-45° and 0°/90° straight filament patterns. A cantilever beam (Figure 14a), a Z-shaped part (Figure 14b), and the previously-used MBB structure are employed for this purpose. Table 1 shows the different optimization parameters used in this study. Besides, the filament width (w), maximum allowed gap (l_{max}), thickness (t), two-layer $(n = 2)$ assumption, convergence tolerance (ag_1, ag_2) and all the material parameters are kept from the previous section. The penalty coefficient is set to ϵ_p=10 and ν_a is set closer to one: $\nu^a = 0.99$, producing the stiffness components' evolution depicted in Figure 15.
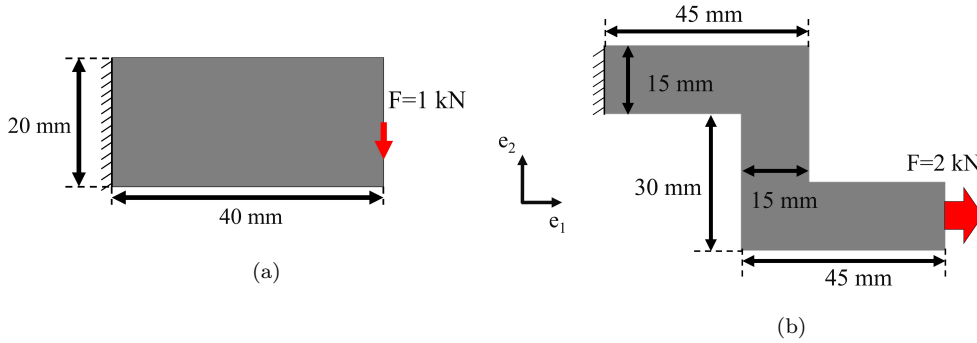

Figure 14: Example structures for Filament Path Optimization. (a) Cantilever beam, (b) Z-shaped part

Table 1: Parameters for optimizing the example structures

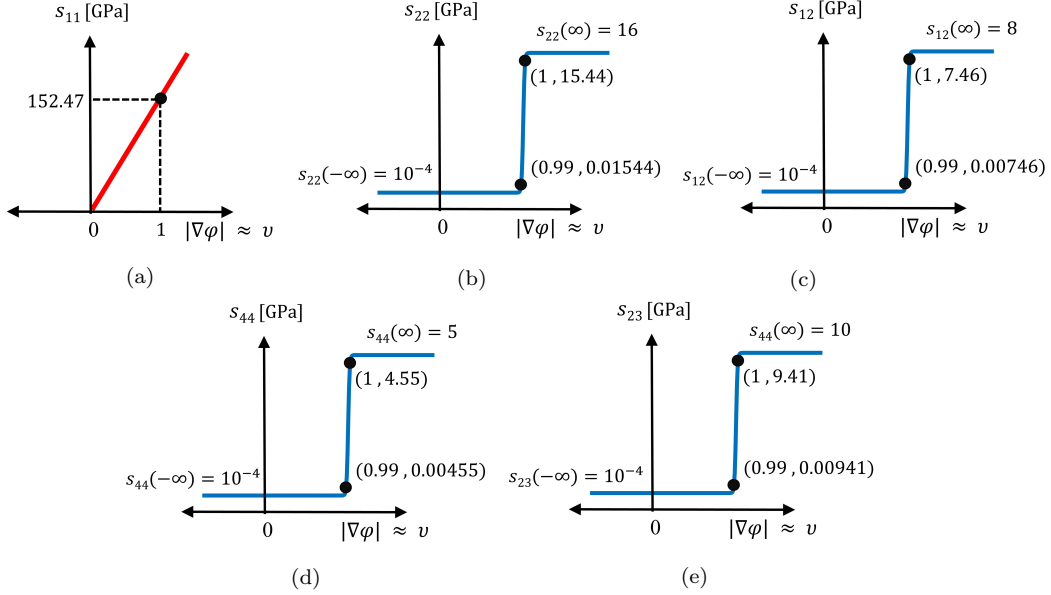|	MBB	Cantilever	Z-Part
Finite Elements	1024	2048	4032
Patches $P_x \times P_y$	$2 \times 2 = 4$	$4 \times 2 = 8$	$5 \times 3 = 15$
Control Points $CP_x \times CP_y$	$5 \times 5 = 25$	$7 \times 5 = 35$	$8 \times 6 = 48$
Design Variables $CP_x \times CP_y \times 2$	50	70	96
Initial Design $\alpha_1^{in}/\alpha_2^{in}$	61.8°/14.3°	18°/-18°	-3.79°/-61.24°

Figure 15: Evolution of the five stiffness parameters s_{11}, s_{22}, s_{12}, s_{44} and s_{23} for the assumed material properties and ν^a=0.99. Only s_{11} is significant before inter-filament fusion. The other components $s_{22}, s_{12}, s_{44}, s_{23}$ are very low for $\nu \leq \nu_a$.

The minimization problem is solved and the optimized filaments are shown in Figures 16 and 17. For clarity, the figures depict the filament paths with a constant width of w=0.6 mm. Table 2 reports the filament path optimization results, also facilitating a comparison between the optimized and standard straight filament patterns using ratios c_f/c_{in}, $c_f/c_{45/\text{-}45}$ and $c_f/c_{0/90}$. The ratio c_f/c_{in} measures the compliance reduction due to curvilinear filaments relative to the initial straight filament design, indicating the benefit of printing curvilinear filaments. On the other hand, the ratios $c_f/c_{45/\text{-}45}$ and $c_f/c_{0/90}$ denote the compliance reduction by optimized filaments relative to the 45°/-45° and 0°/90° straight filaments, respectively, indicating the overall advantage of optimized filament designs over the standard filament patterns.
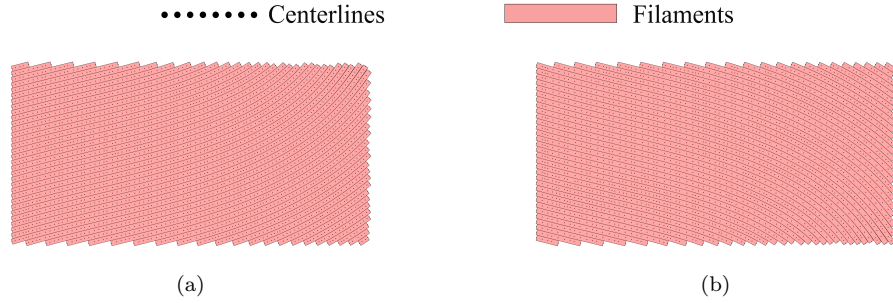
Figure 16: Optimized filament paths in cantilever. (a) Filament Layout-1 (b) Filament Layout-2. Filament paths depicted with a constant width of $w = 0.6$ mm
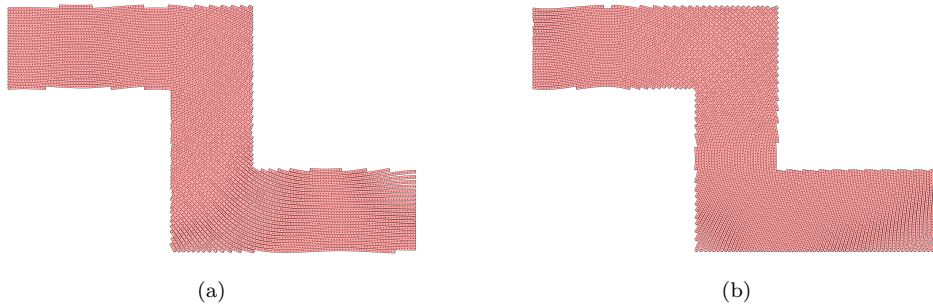

Figure 17: Optimized filament paths in Z-shaped part. (a) Filament Layout-1 (b) Filament Layout-2. Filament paths depicted with a constant filament width of $w = 0.6$ mm

Curvilinear filaments vary the material orientations point-wise, locally exploiting the anisotropy to tailor the mechanical properties in different directions. Their significance is better realized with complex geometries like Z-shaped part, as evident from the compliance reduction $c_{\mathrm{f}}/c_{\mathrm{in}}$ in Table 2. While the MBB beam and the cantilever already show 15% ($c_{\mathrm{f}}/c_{\mathrm{in}} = 0.85$) and 12% ($c_{\mathrm{f}}/c_{\mathrm{in}} = 0.88$) compliance reductions due to curvilinear filaments, the Z-shaped part reaches a higher reduction of 28%. Furthermore, the optimized filament paths offer promising benefits over the standard patterns,

38

thanks to the strong anisotropy in the assumed material. On average, the compliance of the optimum solutions are at least twice as better as the compliance of 45°/-45° and 0°/90° straight filament patterns.

Table 2: Optimized solutions and comparison to standard straight filament patterns. $\alpha_1^{in}/\alpha_2^{in}$: Layer angles at starting point; c_{in} : Compliance at starting point; c_f : Final compliance; T : Computational time; ν^{max} : Maximum volume ratio; ν^{min} : Minimum volume ratio; $c_{45/-45}$: Compliance of part with two layers at 45°and -45°; $c_{0/90}$: Compliance of part with two layers at 0° and 90°

		MBB	Cantilever	Z-Part
Final Solution	$\dfrac{c_f}{c_{in}}$	0.85	0.88	0.72
	ν_1^{max}/ν_2^{max}	1.024/1.042	1.011/1.011	1.01/1.008
	ν_1^{min}/ν_2^{min}	0.92/0.99	0.94/0.94	0.58/0.75
	T [min]	6	8	21
Optimized Solutions Vs straight patterns	$\dfrac{c_f}{c_{45/-45}}$	0.45	0.25	0.25
	$\dfrac{c_f}{c_{0/90}}$	0.49	0.49	0.66

Nevertheless, the ratios c_f/c_{in}, $c_f/c_{45/-45}$ and $c_f/c_{0/90}$ offer only reasonable estimations of the improvements attainable from optimized filament paths. The exact benefits of preferring them over the straight filament patterns can be known through a more rigorous approach, in which their performances

are compared after equalizing the quantity of material or the weights in both cases (Tam and Mueller (2017); Khan et al. (2018)).

5.3. Decoupling the filament spacing influence on printing and transverse direction stiffness

This section compares the optimized solutions from the proposed material model with the classical model of Fernandez et al. (2019) that couples the effect of filament spacing on all stiffness components. For the sake of distinguishing both the models, the optimization involving the Fernandez et al. (2019) model is called *Linear Material Optimization (LMO)* and the one using the proposed model is called *Nonlinear Material Optimization (NMO)*, where the terms *linear* and *non-linear* indicate the corresponding transverse stiffness behaviours with filament spacing in both material models.

LMO is performed here, applying the same initial conditions as in Section 5.2. Table 3 reports the LMO results, while Figures 18 and 19 depict the optimized filament paths. Next, the compliance for the LMO filament paths in Figures 18 and 19 are estimated by the proposed (nonlinear) material model. The newly evaluated compliance, called c_{nL}, are then compared against the initial compliance c_{in} and the final compliance c_L from LMO (refer to Table 3).
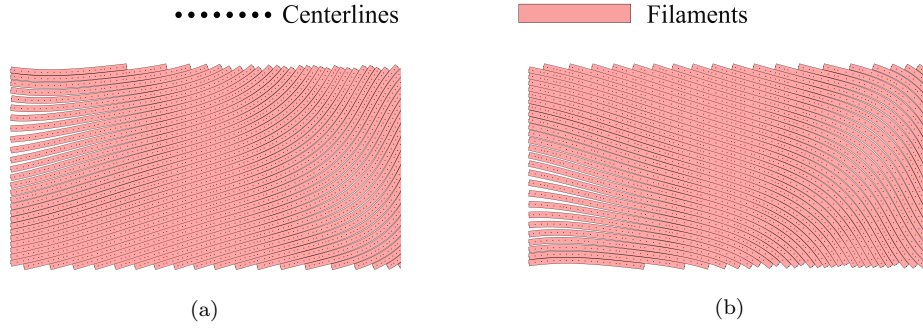
Figure 18: Optimized filament paths in the cantilever structure from LMO. (a) Filament Layout-1 (b) Filament Layout-2. Gaps occur between filaments.
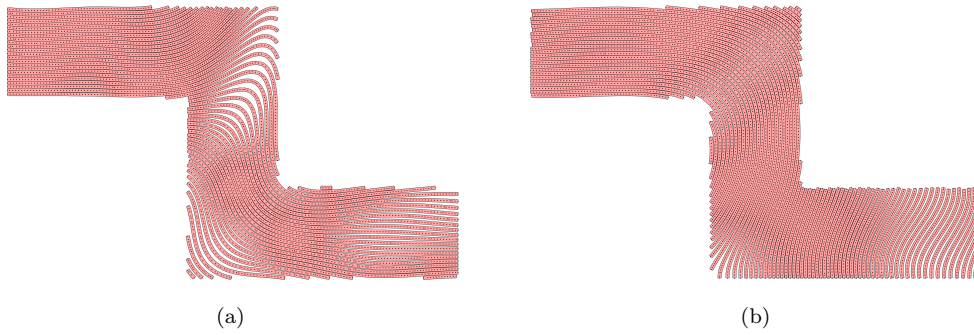

Figure 19: Optimized filament paths in the Z-shaped part from LMO. (a) Filament Layout-1 (b) Filament Layout-2. Gaps occur between filaments.

The optimized filament paths (Figures 18 and 19) and the numerical results (Table 3) from LMO are different from the NMO results in the previous section. Particularly, the LMO filament paths have larger gaps than the NMO filament paths in Figures 16 and 17. The corresponding differences in the compliance assigned by the two material models are inferred from the ratios c_{nL}/c_{in} and c_{nL}/c_{L}. For instance, LMO yielded a compliance reduction of $c_{L}/c_{in} = 0.81$ and 0.62 for the cantilever and Z-shaped part, respectively.

41

Whereas, the proposed nonlinear material model assigned higher compliance to the LMO filament paths with $c_{nL}/c_{in} = 0.95$ and 4.36.

Table 3: Optimized solutions from the LMO and comparison of compliance assigned by the linear and nonlinear material models for filament paths in Figures 18 and 19. c_{in} : compliance at starting point; c_L : final compliance from LMO; ν^{max} : maximum volume ratio; ν^{min} : minimum volume ratio; c_{nL} : compliance assigned by the proposed nonlinear material model

		Cantilever	**Z-Part**
Results	$\dfrac{c_L}{c_{in}}$	0.81	0.62
from			
LMO	ν_1^{max}/ν_2^{max}	1.05/1.05	1.048/1.036
	ν_1^{min}/ν_2^{min}	0.55/0.55	0.35/0.3
Comparison of	$\dfrac{c_{nL}}{c_{in}}$	0.95	4.36
compliance from two			
material models	$\dfrac{c_{nL}}{c_L}$	1.2	7

Thus, larger inter-filament gaps and the reduced compliance result from LMO, which are due to the over-estimated transverse stiffness component at pre-fusion densities, produced, in turn, by the coupled linear variation of all the stiffness components with the filament spacing. In contrast, the proposed material model incorporates a decoupled behaviour by dropping the transverse stiffness rapidly when the filament density is below a given threshold ($\nu_i \leq \nu_a$), which is expected to be a more realistic assumption that leads to closely printed filament solutions from NMO.

The activation points ν_a play a crucial role in the effectiveness of NMO. So far, ν_a was set close to one i.e., $\nu_a \to 1$. For completeness, the influence of varying this material parameter is investigated next.

Role of the activation point ν_a

NMO is done again as in Section 5.2, but with a lower value of ν_a=0.1. Figure 20 shows the corresponding stiffness components' evolution.

The compliance reduction factors of the optimized cantilever and Z-shaped part are now $c_f/c_{in} = 0.81$ and 0.63, respectively. Figures 21 and 22 depict the optimized filament paths from $\nu_a = 0.1$, also comparing them against the solutions of $\nu_a = 0.99$.
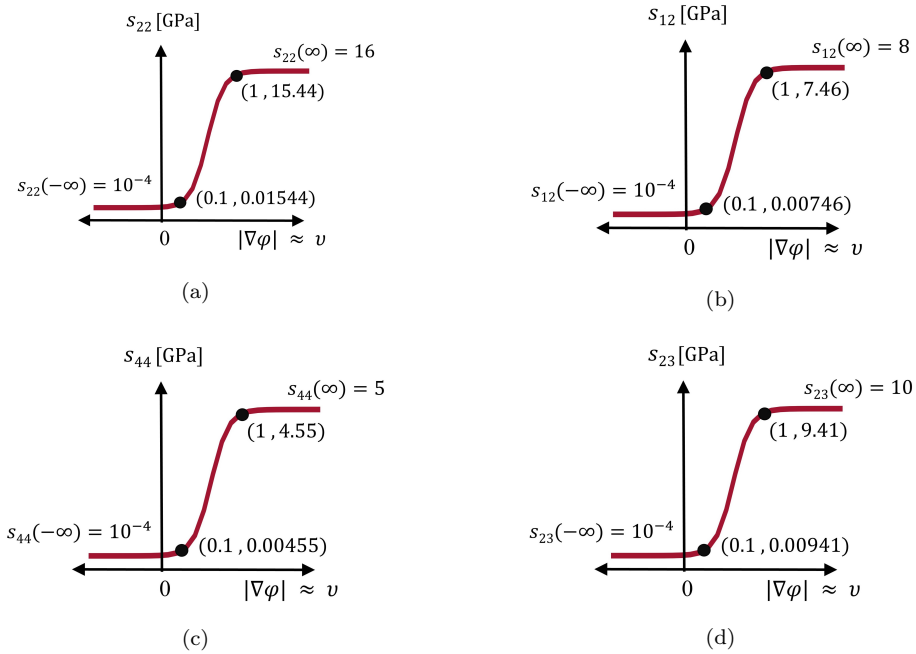

Figure 20: Evolution of the five stiffness parameters s_{22}, s_{12}, s_{44} and s_{23} for the assumed material properties and ν^a=0.1. Before inter-filament fusion, all stiffness components are significant, which is physically unrealistic.

Similar to LMO, NMO with ν^a=0.1 yielded lower compliance reduction factors and larger inter-filament gaps due to the coupled variation of all the stiffness components with the filament spacing. Therefore, to avoid such solutions, the present work assumed $\nu_a \to 1$ and treated the printing and transverse stiffness differently to represent a physically sound phenomenon.
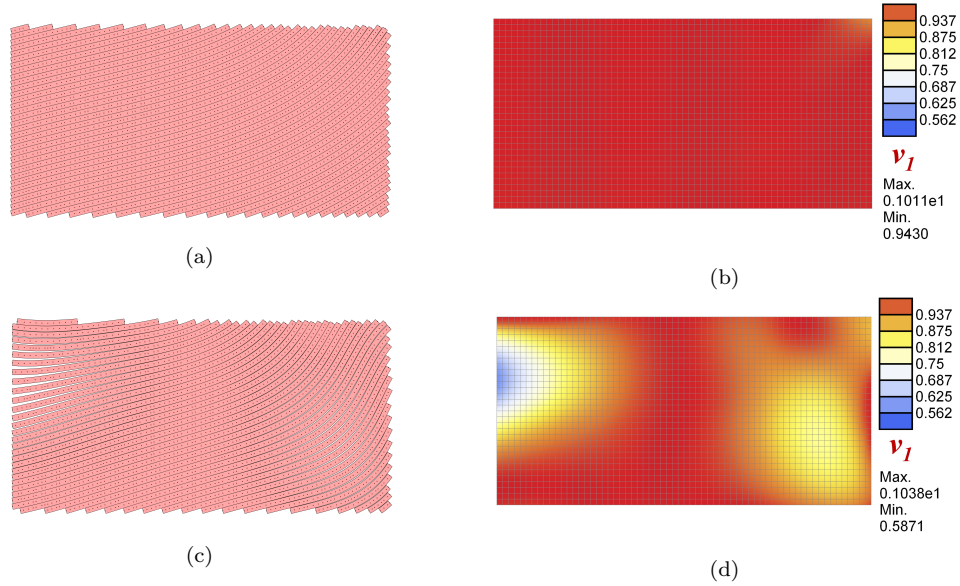

Figure 21: Influence of ν^a in Cantilever. (a) Optimized filament layout-1 with $\nu_a = 0.99$, (b) Volume-ratio plot for filament layout-1 with $\nu_a = 0.99$, (c) Optimized filament layout-1 with $\nu_a = 0.1$, (b) Volume-ratio plot for filament layout-1 with $\nu_a = 0.1$. NMO with $\nu_a = 0.1$ produce inter-filament gaps similar to LMO.

Note that it was also observed that a higher value of ν^a was more likely to cause numerical difficulties during the minimization process because of not feeding the transverse stiffness of distant filaments. Such scenarios produced ill-conditioned stiffness-matrix in the FE procedure that terminated the FEA and, in turn, the minimization process. The gradient based ap-

proaches can avert this issue to a certain extent by limiting the maximum step-size attempted from the initial straight pattern. Differential Evolution, on the other hand, does not allow for this because it searches the entire design space with numerous candidate solutions and is likely to encounter large gaps. For the same reason, while working with Differential Evolution in section 5.1, the value ν^a=0.9 had to be used.
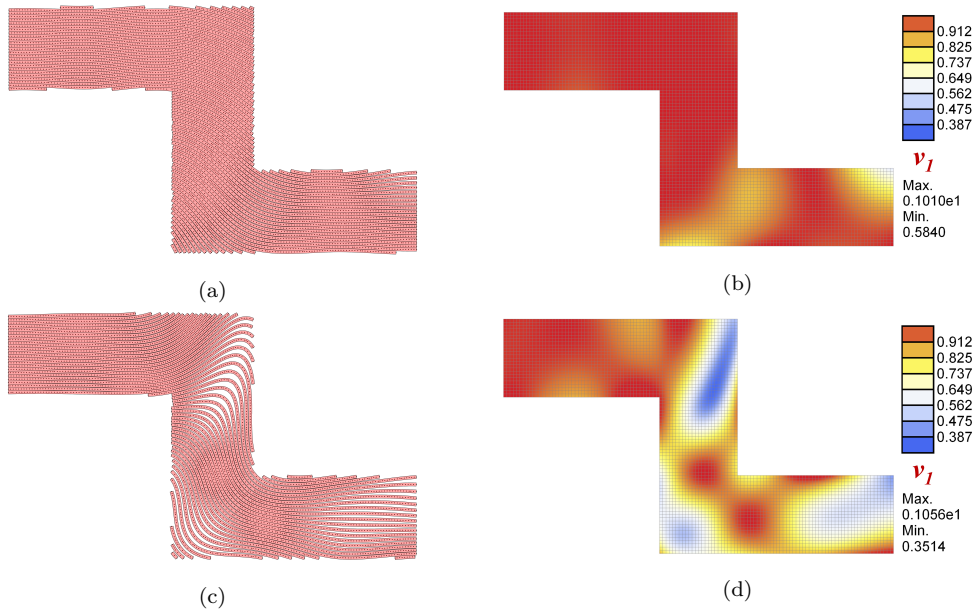

Figure 22: Influence of ν^a in Z-Shaped Part. (a) Optimized filament layout-1 with $\nu_a = 0.99$, (b) Volume-ratio plot for filament layout-1 with $\nu_a = 0.99$, (c) Optimized filament layout-1 with $\nu_a = 0.1$, (b) Volume-ratio plot for filament layout-1 with $\nu_a = 0.1$. NMO with $\nu_a = 0.1$ produce inter-filament gaps similar to LMO.

Observing the significant influence of ν_a on the results, the appropriate choice of this material parameter is therefore crucial and should be ideally identified by experimental calibration.

6. Conclusion and Outlook

This work dealt with the filament path optimization of in-plane FFF structures, where two manufacturing constraints were imposed to obtain production-ready solutions. A significant portion of this work focused on proposing and applying a new material model that incorporated a decoupled variation of the printing and transverse stiffness components with inter-filament spacing. The filament paths optimized using the proposed model were observed to be more realistic, containing a lower proportion of inter-filament gaps than those that resulted from a model that assumed a coupled linear variation in all its stiffness components.

A second contribution compared the two-step gradient-based approach and the Differential Evolution for the filament path optimization. The two-step gradient-based approach achieved final compliance closer to Differential Evolution at a lower computational cost, proving to be more efficient and a preferable choice for this type of problem. A further reason to employ the gradient-based approach is the appearance of numerical issues in Differential Evolution when the stiffness components are activated close to inter-filament fusion (i.e., $\nu_a \to 1$).

Following this work, verifying the conclusions drawn in this numerical work through experimental testing and comparison against classical printing patterns constitutes future work of high practical relevance. Another point of immediate interest is the extension of the proposed approach to 3D problems.

Acknowledgements

References

Ahn, S.H., Montero, M., Odell, D., Roundy, S., Wright, P.K., 2002. Anisotropic material properties of fused deposition modeling abs. Rapid prototyping journal 8, 248–257.

Alaimo, G., Marconi, S., Costato, L., Auricchio, F., 2017. Influence of meso-structure and chemical composition on fdm 3d-printed parts. Composites Part B: Engineering 113, 371–380.

Ali, M., Zhu, W., 2013. A penalty function-based differential evolution algorithm for constrained global optimization. Computational Optimization and Applications 54, 707–739.

Amstutz, S., 2010. A penalty method for topology optimization subject to a pointwise state constraint. ESAIM: Control, Optimisation and Calculus of Variations 16, 523–544.

Amstutz, S., Novotny, A., de Souza Neto, E., 2012. Topological derivative-based topology optimization of structures subject to drucker–prager stress

constraints. Computer Methods in Applied Mechanics and Engineering 233, 123–136.

Amstutz, S., Novotny, A.A., 2010. Topological optimization of structures subject to von mises stress constraints. Structural and Multidisciplinary Optimization 41, 407–420.

Bartels, R.H., Beatty, J.C., Barsky, B.A., 1995. An introduction to splines for use in computer graphics and geometric modeling. Morgan Kaufmann.

Blok, L.G., Longana, M.L., Yu, H., Woods, B.K., 2018. An investigation into 3d printing of fibre reinforced thermoplastic composites. Additive Manufacturing 22, 176–186.

Blom, A.W., Setoodeh, S., Hol, J.M., Gürdal, Z., 2008. Design of variable-stiffness conical shells for maximum fundamental eigenfrequency. Computers & structures 86, 870–878.

Brampton, C.J., Wu, K.C., Kim, H.A., 2015. New optimization method for steered fiber composites using the level set method. Structural and Multidisciplinary Optimization 52, 493–505.

Brenken, B., Barocio, E., Favaloro, A., Kunc, V., Pipes, R.B., 2018. Fused filament fabrication of fiber-reinforced polymers: A review. Additive Manufacturing 21, 1–16.

Brett Champion, A.S., 2008. Constrained optimization. https://library.wolfram.com/infocenter/ID/8506/, Last Visited: 26-11-2021.

Catapano, A., Desmorat, B., Vannucci, P., 2015. Stiffness and strength optimization of the anisotropy distribution for laminated structures. Journal of Optimization Theory and Applications 167, 118–146.

Cuan-Urquizo, E., Barocio, E., Tejada-Ortigoza, V., Pipes, R.B., Rodriguez, C.A., Roman-Flores, A., 2019. Characterization of the mechanical properties of fff structures and materials: A review on the experimental, computational and theoretical approaches. Materials 12, 895.

Durgun, I., Ertan, R., 2014. Experimental investigation of fdm process for improvement of mechanical properties and production cost. Rapid Prototyping Journal 20, 228–235.

Duvaut, G., Terrel, G., Léné, F., Verijenko, V., 2000. Optimization of fiber reinforced composites. Composite Structures 48, 83–89.

Esposito, L., Cutolo, A., Barile, M., Lecce, L., Mensitieri, G., Sacco, E., Fraldi, M., 2019. Topology optimization-guided stiffening of composites realized through automated fiber placement. Composites Part B: Engineering 164, 309–323.

Fayazbakhsh, K., Movahedi, M., Kalman, J., 2019. The impact of defects on tensile properties of 3d printed parts manufactured by fused filament fabrication. Materials Today Communications 18, 140–148.

Fernandez, F., Compel, W.S., Lewicki, J.P., Tortorelli, D.A., 2019. Optimal design of fiber reinforced composite structures and their direct ink write fabrication. Computer Methods in Applied Mechanics and Engineering 353, 277–307.

Gämperle, R., Müller, S.D., Koumoutsakos, P., 2002. A parameter study for differential evolution. Advances in intelligent systems, fuzzy systems, evolutionary computation 10, 293–298.

Gaynor, A.T., 2015. Topology optimization algorithms for additive manufacturing. Ph.D. thesis. Johns Hopkins University.

Ghiasi, H., Fayazbakhsh, K., Pasini, D., Lessard, L., 2010. Optimum stacking sequence design of composite materials part ii: Variable stiffness design. Composite structures 93, 1–13.

Ghiasi, H., Pasini, D., Lessard, L., 2009. Optimum stacking sequence design of composite materials part i: Constant stiffness design. Composite Structures 90, 1–11.

Giorgio, I., Ciallella, A., Scerrato, D., 2020. A study about the impact of the topological arrangement of fibers on fiber-reinforced composites: some guidelines aiming at the development of new ultra-stiff and ultra-soft metamaterials. International Journal of Solids and Structures 203, 73–83.

Hodgson, G., Ranellucci, A., Moe, J., 2011. Slic3r manual. `https://manual.slic3r.org/`, Last Visited: 14-03-2022.

Hoglund, R., Smith, D., 2016. Continuous fiber angle topology optimization for polymer fused filament fabrication, in: Proceedings of the 27th annual international solid freeform fabrication symposium, austin, TX, USA, pp. 8–10.

Honda, S., Narita, Y., 2011. Vibration design of laminated fibrous composite

plates with local anisotropy induced by short fibers and curvilinear fibers. Composite Structures 93, 902–910.

Honda, S., Narita, Y., 2012. Natural frequencies and vibration modes of laminated composite plates reinforced with arbitrary curvilinear fiber shape paths. Journal of Sound and Vibration 331, 180–191.

Honda, S., Narita, Y., Sasaki, K., 2009. Maximizing the fundamental frequency of laminated composite plates with optimally shaped curvilinear fibers. Journal of system design and dynamics 3, 867–876.

Hou, Z., Tian, X., Zhang, J., Zheng, Z., Zhe, L., Li, D., Malakhov, A.V., Polilov, A.N., 2021. Optimization design and 3d printing of curvilinear fiber reinforced variable stiffness composites. Composites Science and Technology 201, 108502.

Huang, G., Wang, H., Li, G., 2016. An efficient reanalysis assisted optimization for variable-stiffness composite design by using path functions. Composite Structures 153, 409–420.

Huang, J., Haftka, R., 2005. Optimization of fiber orientations near a hole for increased load-carrying capacity of composite laminates. Structural and Multidisciplinary Optimization 30, 335–341.

Hyer, M.W., Charette, R., 1991. Use of curvilinear fiber format in composite structure design. AIAA journal 29, 1011–1015.

Izzi, M.I., Catapano, A., Montemurro, M., 2021. Strength and mass optimisation of variable-stiffness composites in the polar parameters space. Structural and Multidisciplinary Optimization 64, 2045–2073.

51

Kalamkarov, A.L., Andrianov, I.V., Danishevs'kyy, V.V., 2009. Asymptotic homogenization of composite materials and structures. Applied Mechanics Reviews 62.

Khan, S., Fayazbakhsh, K., Fawaz, Z., Nik, M.A., 2018. Curvilinear variable stiffness 3d printing technology for improved open-hole tensile strength. Additive Manufacturing 24, 378–385.

Kim, B.C., Potter, K., Weaver, P.M., 2012. Continuous tow shearing for manufacturing variable angle tow composites. Composites Part A: Applied Science and Manufacturing 43, 1347–1356.

Kiyono, C., Silva, E., Reddy, J., 2017. A novel fiber optimization method based on normal distribution function with continuously varying fiber path. Composite structures 160, 503–515.

Kollar, L.P., Springer, G.S., 2003. Mechanics of composite structures. Cambridge university press.

Korelc, J., 2007. Acegen and acefem manual. `http://symech.fgg.uni-lj.si/`, Last Visited: 03-1-2022.

Le, C., Norato, J., Bruns, T., Ha, C., Tortorelli, D., 2010. Stress-based topology optimization for continua. Structural and Multidisciplinary Optimization 41, 605–620.

Legrand, X., Kelly, D., Crosky, A., Crépin, D., 2006. Optimisation of fibre steering in composite laminates using a genetic algorithm. Composite structures 75, 524–531.

Lemaire, E., Zein, S., Bruyneel, M., 2015. Optimization of composite structures with curved fiber trajectories. Composite Structures 131, 895–904.

Li, L., Sun, Q., Bellehumeur, C., Gu, P., 2002. Composite modeling and analysis for fabrication of fdm prototypes with locally controlled properties. Journal of manufacturing processes 4, 129–141.

Liu, J., Gaynor, A.T., Chen, S., Kang, Z., Suresh, K., Takezawa, A., Li, L., Kato, J., Tang, J., Wang, C.C., et al., 2018. Current and future trends in topology optimization for additive manufacturing. Structural and multidisciplinary optimization 57, 2457–2483.

Liu, J., To, A.C., 2017. Deposition path planning-integrated structural topology optimization for 3d additive manufacturing subject to self-support constraint. Computer-Aided Design 91, 27–45.

Liu, J., Yu, H., 2017. Concurrent deposition path planning and structural topology optimization for additive manufacturing. Rapid Prototyping Journal .

Lopes, C., Gürdal, Z., Camanho, P., 2008. Variable-stiffness composite panels: Buckling and first-ply failure improvements over straight-fibre laminates. Computers & Structures 86, 897–907.

Lopes, C.S., Camanho, P.P., Gürdal, Z., Tatting, B.F., 2007. Progressive failure analysis of tow-placed, variable-stiffness composite panels. International Journal of Solids and Structures 44, 8493–8516.

Lozano, G.G., Tiwari, A., Turner, C., 2018. A design algorithm to model fibre

paths for manufacturing of structurally optimised composite laminates. Composite Structures 204, 882–895.

Malakhov, A., Polilov, A., 2016. Design of composite structures reinforced curvilinear fibres using fem. Composites Part A: Applied Science and Manufacturing 87, 23–28.

Marschner, S., Shirley, P., 2015. Fundamentals of computer graphics. CRC Press.

Monaldo, E., Marfia, S., 2021. Multiscale technique for the analysis of 3d-printed materials. International Journal of Solids and Structures 232, 111173.

Montemurro, M., Catapano, A., 2017. On the effective integration of manu-facturability constraints within the multi-scale methodology for designing variable angle-tow laminates. composite structures 161, 145–159.

Nagendra, S., Kodiyalam, S., Davis, J., Parthasarathy, V., 1995. Optimiza-tion of tow fiber paths for composite design, in: 36th structures, structural dynamics and materials conference, p. 1275.

Ngim, D., Liu, J.S., Soar, R., 2007. Design optimization for manufacturability of axisymmetric continuum structures using metamorphic development. International journal of solids and structures 44, 685–704.

Nocedal, J., Wright, S., 2006. Numerical optimization. Springer Science & Business Media.

Oleksandr, R., 2016. Step monitor option in differential evolution. Wolfram Mathematica Stack Exchange. https://mathematica.stackexchange.com/questions/114796/step-monitor-option-in-differentialevolution, Last Visited: 27-11-2021.

Price, K., Storn, R.M., Lampinen, J.A., 2006. Differential evolution: a practical approach to global optimization. Springer Science & Business Media.

Roberge, J., Norato, J., 2018. Computational design of curvilinear bone scaffolds fabricated via direct ink writing. Computer-Aided Design 95, 1–13.

Rodríguez, J.F., Thomas, J.P., Renaud, J.E., 2001. Mechanical behavior of acrylonitrile butadiene styrene (abs) fused deposition materials. experimental investigation. Rapid Prototyping Journal 7, 148–158.

Sá, Â.A., Andrade, A.O., Soares, A.B., Nasuto, S.J., 2008. Exploration vs. exploitation in differential evolution, in: AISB 2008 Convention Communication, Interaction and Social Intelligence, Citeseer. p. 57.

Setoodeh, S., Abdalla, M.M., IJsselmuiden, S.T., Gürdal, Z., 2009. Design of variable-stiffness composite panels for maximum buckling load. Composite structures 87, 109–117.

Stegmann, J., Lund, E., 2005. Discrete material optimization of general composite shell structures. International Journal for Numerical Methods in Engineering 62, 2009–2027.

Storn, R., Price, K., 1997. Differential evolution–a simple and efficient heuristic for global optimization over continuous spaces. Journal of global optimization 11, 341–359.

Storn, R.M., Price, K., 1995. Differential Evolution - A simple and efficient adaptive scheme for global optimization over continuous spaces. Technical Report. International Computer Science Institute.

Tam, K.M.M., Mueller, C.T., 2017. Additive manufacturing along principal stress lines. 3D Printing and Additive Manufacturing 4, 63–81.

Tatting, B.F., Gürdal, Z., Jegley, D., 2002. Design and manufacture of elastically tailored tow placed plates. NASA STI report series .

Tekinalp, H.L., Kunc, V., Velez-Garcia, G.M., Duty, C.E., Love, L.J., Naskar, A.K., Blue, C.A., Ozcan, S., 2014. Highly oriented carbon fiber–polymer composites via additive manufacturing. Composites Science and Technology 105, 144–150.

Vyavahare, S., Teraiya, S., Panghal, D., Kumar, S., 2020. Fused deposition modelling: A review. Rapid Prototyping Journal .

Wu, Z., Weaver, P.M., Raju, G., Kim, B.C., 2012. Buckling analysis and optimisation of variable angle tow composite plates. Thin-walled structures 60, 163–172.

Yamanaka, Y., Todoroki, A., Ueda, M., Hirano, Y., Matsuzaki, R., et al., 2016. Fiber line optimization in single ply for 3d printed composites. Open Journal of Composite Materials 6, 121.

Zegard, T., Paulino, G.H., 2016. Bridging topology optimization and additive manufacturing. Structural and Multidisciplinary Optimization 53, 175–192.

Zhang, P., Liu, J., To, A.C., 2017. Role of anisotropic properties on topology optimization of additive manufactured load bearing structures. Scripta Materialia 135, 148–152.

Appendix A. Control parameter tuning in differential evolution

Table A.4 shows four stages of applying Differential Evolution to the minimization problem in Eq.(12). In each stage, multiple trials are conducted using various combinations of cross-probability C_r, population size SP and maximum generations G_{max}, recording for each combination, the following

Table A.4: Tuning of control parameters. C_r : crossover probability; G_{max} : maximum generations; SP : population size of candidate solutions; p_b : best value of cost function reached by candidate solutions; T : computational time; G : completed number of generations before termination

Stages	C_r	G_{max}	SP	p_b	T [min]	G
	0.99	100	50	7.3×10^9	18	100
I	0.5	100	50	1.8×10^7	20	100
	0.01	100	50	5.6×10^6	21	100
II	0.5	250	50	1.3×10^7	24	125
	0.01	250	50	3.3×10^6	59	250
	0.01	250	80	1.1×10^6	72	250
III	0.01	250	125	0.79×10^6	114	250
	0.01	250	170	4×10^6	150	250
	0.01	500	135	723	234	500
IV	0.01	1000	135	208	522	1000
	0.01	2000	135	143	960	2000
	0.01	**3000**	**135**	**136.45**	**1800**	**3000**

quantities : the best penalized cost function p_b attained by the candidate solutions, the number of generations G completed before termination, and the corresponding computational time T. Based on the results of each trial, the control parameters C_r, SP and G_{max} are progressively tuned to reach the final set of values that fetch the optimum solution.

Fixing the maximum generations to $G_{max} = 100$, and the population size to $SP = 50$, Stage-I applied three cross-probabilities that are representative of its entire range: $C_r = 0.01$, 0.5 and 0.99. On one extreme, the value $C_r = 0.01$ favours exploration of the design space, whereas $C_r = 0.99$ exploits a potential candidate solution and refines it towards the minimum point. The median value $C_r = 0.5$ balances both the exploration and exploitation factors in equal proportion. Anyhow, all the three trials completed G=100 generations, yielding very high values of penalized cost function p_b that indicated severe constraint violations.

Stage-II allowed the same set of candidate solutions to evolve and explore upto maximum generation of $G_{max} = 250$. Only cross-probabilities C_r=0.5 and C_r=0.01 were used since $C_r = 0.99$ yielded unsatisfactory results in the previous stage. The trial with C_r=0.5 converged upon a single solution and prematurely terminated the minimization process at $G = 125$ generations, yielding a penalized cost function $p_b = 1.3 \times 10^7$. Whereas, C_r=0.01 enabled the exploration of the design space until maximum generation G_{max} was reached, attaining a significantly lower cost function p_b at a higher computation effort (T=59 minutes).

Stage-III further explored the design space using larger population sizes: SP=80, 125 and 170, while retaining $G_{max} = 250$ and C_r=0.01 to catalyze

the design space exploration. Compared to the results from SP=50, the population size SP=80 reached a lower cost function of $p_b = 1.1 \times 10^6$, which was in turn surpassed by the population size SP=125 to reach $p_b = 0.79$ $\times 10^6$. The cost function did not reduce further when the population size was increased to $SP = 170$. Whereas, the computational time T increased, as expected, since a larger population size needs additional FE evaluations.

Based on the previous results, Stage IV parameters were set to $C_r = 0.01$, SP =135 and $G_{max} = 500$ to 3000. The final cost function values p_b dropped with an increase of maximum generations G_{max}, eventually reaching p_b=136.45 in G=3000 generations. Figure A.23 shows the history of the best penalized cost function p_b against the number of generations G. The parameter tuning process was stopped here, witnessing a decreasing reduction rate in p_b, which indicated that a (near) minimum had been found after sufficient exploration of the design space.
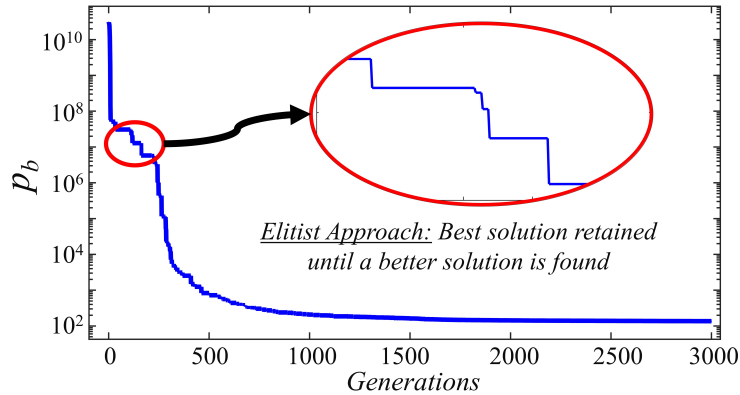

Figure A.23: Decrease in the best penalized cost function p_b as generations increase. Solutions with best p_b retained for multiple generations until a better solution is found (elitist approach).